



25 **ABSTRACT**

26 High-velocity friction (HVF) experiments on serpentinite under conditions equivalent  
27 to large amounts of earthquake slip produced large volumes of water vapor derived from  
28 the frictional-heating-induced dehydration of serpentinite. Fourier Transform Infrared  
29 (FTIR) and thermogravimetry (TG)-Differential Scanning Calorimetry (DSC)  
30 microspectroscopic analyses show that the water in the slip zone and its bounding zones  
31 was released due to dehydration during the HVF experiments. Our experimental results  
32 demonstrate that (i) the run product consists of ~10 wt.% molten materials with  
33 abundant vesicles and ~90 wt.% fine-grained clasts; (ii) both serpentine and olivine  
34 minerals were melted during high-velocity slip (1.1–1.3 m/s); (iii) rapid serpentine  
35 dehydration occurred in a zone of up to ~3 mm wide, including the slip zone and its  
36 bounding zones, accompanying frictional melting during high-velocity slip; and (iv) no  
37 distinct dehydration or frictional melting occurred during low-velocity slip (<0.4 m/s).  
38 These findings show that dehydration reactions of serpentine can be caused by frictional  
39 heating that accompanies frictional melting in the slip zone, and by the rapid diffusion  
40 of frictional heat from the main slip zone to a wide zone bounded by the coseismic slip  
41 plane during seismic faulting. The present results reveal that the thermal pressurization  
42 caused by the dehydration of serpentine and frictional melting is a main mechanism that  
43 may lead to the dynamic weakening of seismogenic faults, thereby facilitating seismic  
44 slip during large earthquakes in subduction zones and along intracontinental faults that  
45 contain abundant hydrous minerals.

46

47 **Keywords:** dehydration, serpentinite, high-velocity slip, fault strength, dynamic

48 weakening of seismogenic fault, thermal pressurization

49

## 50 **1. Introduction**

51

52 Thermal pressurization has been proposed as a major mechanism of lowering the  
53 dynamic strength of faults during earthquake slip [e.g., Sibson, 1973; Lachenbruch,  
54 1980; Andrews, 2002; Wibberley and Shimamoto, 2005]. A commonly invoked  
55 mechanism of thermal pressurization in this regard is a reduction in effective normal  
56 stress induced by the sudden increase in pore pressure that arises from the release of  
57 fluid via dehydration reactions [e.g., Meade and Jeanloz, 1991; Tibi et al., 2002]. In  
58 recent years, many experimental studies have suggested that thermal pressurization may  
59 result from mineral decomposition, such as the dehydration of serpentine or kaolinite  
60 [e.g., Hirose and Bystricky, 2007; Brantut et al., 2008; Viti and Hirose, 2010; Kohli et  
61 al., 2011], the decarbonation of calcite or siderite [Han et al., 2007, 2010], and the  
62 dehydration of gypsum [Brantut et al., 2011]. Observations of natural seismogenic fault  
63 cores that contain fault gouges also support the supposition that dehydration reactions  
64 occur during seismic faulting [e.g., Famin et al., 2008; Hamada et al., 2009, 2011].

65 Serpentine is closely associated with transform faults [e.g., Christensen, 1972;  
66 Francis, 1981; Moore and Rymer, 2007] and with seismogenic faults within subduction  
67 zones [Ulmer and Trommsdorff, 1995]; indeed, the presence of serpentine minerals is  
68 considered to facilitate creep along the San Andreas Fault [Moore and Rymer, 2007],  
69 thereby explaining its low fault strength [Wibberley, 2007]. In numerical modeling, heat  
70 diffusion is considered an important coupling factor of thermal pressurization, which

71 occurs normal to the slip zone [Brantut et al., 2010]. Should serpentine dehydration  
72 occur due to frictional heating along seismogenic faults and should heat diffusion occur  
73 within a wide dehydration reaction zone bounded by the slip zone during earthquake slip,  
74 it is likely that a considerable volume of water would be released from serpentine-rich  
75 slip zones and their bounding zones. Thus, it is proposed that a rapid dehydration  
76 reaction involving serpentine would induce a sudden increase in fluid pressure that  
77 would simultaneously act to reduce the effective normal stress and markedly weaken the  
78 dynamic strength of seismogenic faults during seismic faulting.

79 To test this hypothesis, a low- to high-velocity rotary shear test apparatus [Lin, 2008]  
80 was used to conduct uniaxial high-velocity friction (HVF) experiments under conditions  
81 equivalent to large earthquake slip with various slip rates, using natural serpentinite  
82 samples from Nagano Prefecture, Japan. This paper describes the results of these  
83 experiments, which showed the instantaneous dehydration of serpentinite due to  
84 frictional heating along the simulated fault and heat diffusion within a wide zone  
85 bounded by the slip zone.

86

## 87 **2. Experimental Procedure and Conditions**

88

### 89 ***2.1. Test Equipment***

90

91 All of the present experiments on frictional-heating-induced hydration of serpentine  
92 were performed under dry conditions using a rotary-shear low- to high-velocity  
93 frictional test machine installed at Shizuoka University, Japan (Fig. 1). This machine

94 contains two testing devices: a uniaxial rotary-shear low- to high-velocity friction device  
95 that lacks a hydraulic pressure vessel [as used by Lin and Shimamoto, 1998], and a  
96 hydraulic friction apparatus with a controlling device for high pore-water pressure,  
97 attached to the uniaxial rotary-shear low- to high-velocity friction device (Figs 1 and 2).  
98 This device has a wide range of slip rates, from <10 cm/yr to 10 m/s, yielding  
99 mechanical data such as torque, the frictional coefficient, amount of axial shortening,  
100 normal stress and shear stress, pore-water pressure, frictional melt temperature, and  
101 displacement. The test equipment can be used to apply normal stresses up to  
102 approximately 100 MPa, close to the typical uniaxial strength of crystalline rocks,  
103 provided that anvil-shaped specimens are used. In practical use, however, it is only  
104 possible to apply normal stresses of <15 MPa because of the severe thermal fracturing  
105 of unconfined specimens that occurs upon frictional heating.

106

## 107 ***2.2. Experimental Conditions***

108

109 Serpentine samples for the experiments, collected from Nagano Prefecture, central  
110 Japan, were free of visible cracks and consisted of ~65% antigorite and ~35% olivine,  
111 along with trace amounts of mafic minerals (Fig. 3).

112 Ten HVF experiments were performed at room temperature under dry conditions and  
113 with equivalent slip rates [Shimamoto and Tsutsumi, 1994; Lin and Shimamoto, 1998]  
114 of 1.10–1.31 m/s and normal stresses of 2–9 MPa (Table 1). In such experiments, the  
115 slip rate varies from the inner to outer circumferences of the sample, so we used the  
116 equivalent slip rate ( $V_{eq}$ ), which is defined as  $V_{eq}$  multiplied by the area of sliding

117 equals the rate of frictional work. Assuming a constant frictional coefficient over the  
118 sliding surface,  $V_{eq}$  for a cylindrical specimen of diameter  $r$  is given by

$$119 \quad V_{eq} = 4/3 \pi r R$$

120 where  $R$  is the revolution rate of the motor [Shimamoto and Tsutsumi, 1994].

121 Low-velocity (0.35–0.4 m/s) friction (LVF) experiments were conducted for comparison  
122 with the results of the HVF experiments (Table 2). A pair of cylindrical specimens (25  
123 mm in diameter and 50 mm in length) was used in each experiment, with the circular  
124 interface between the two specimens being set as the slip plane (Fig. 2). The sliding  
125 surfaces were polished with 1500# SiC powders. Because large normal stresses could  
126 not be applied to the simulated fault due to the limitations of the experimental apparatus,  
127 the HVF experiments were run over a period of ~15–40 sec, corresponding to  
128 displacements of 20–50 m. These displacements are comparable with those recorded  
129 during large-magnitude earthquakes (e.g., maximum displacements of 15–30 m have  
130 been reported for the 2001  $M_w$  7.8 Kunlun earthquake [Lin et al., 2002], the 2004  $M_w$   
131 9.0 Sumatra–Andaman earthquake [Subarya et al., 2006], and the 2011  $M_w$  9.0 Offshore  
132 Tohoku (Japan) earthquake [Yagi and Fukahata, 2011]). In contrast, the total  
133 displacements over a period of ~15–40 sec in the LVF experiments were calculated to  
134 be 5–15 m. The frictional energy expended per unit area in the experiments under a slip  
135 rate of ~1 m/s and a large displacement of up to 50 m is similar to that expended during  
136 a medium- to large-magnitude crustal earthquake [O’Hara et al., 2006], at least in terms  
137 of slip velocity and stress drop [Kanamori and Brodsky, 2004].

138 Serpentine dehydration phenomena were directly observed during the HVF  
139 experiments (1.10–1.31 m/s) through a transparent window cover on the experimental

140 apparatus (Fig. 4). The simulated fault began to produce water vapor and dust within 0.2  
141 sec of the initiation of fault motion (Fig. 4a). Water vapor, accompanied by sparks and  
142 red melt material, was sprayed out from the slip zone, with some instantaneously  
143 cooling to water droplets (0.1–5.0 mm in diameter) on the transparent window cover  
144 (Fig. 4b–d). The ejection of water vapor from the simulated fault continued until the end  
145 of each experiment, with the droplets on the window cover forming a band of 3–7 mm  
146 in width (Fig. 4b–d). In contrast, such water vapor and water droplets were not observed  
147 during the LVF experiments.

148

### 149 **3. Results**

150

#### 151 ***3.1. Microstructures of Run Products***

152

153 The slip zones that formed during the experiments ranged in width from 0.1 to 2.0  
154 mm, consisting of numerous fractured fragments of olivine within a very fine-grained  
155 matrix that was too fine to enable the identification of minerals (Figs 5 and 6), even by  
156 powder X-ray diffraction analysis. The olivine crystals abutting the slip zone were  
157 generally fractured, with numerous cracks infilled by molten run products containing  
158 fine-grained clasts, forming complex network veins branching from the main slip zone  
159 (Fig. 5a). These veins resemble natural pseudotachylyte veins in their geometry and  
160 morphology [Lin, 2008]. In contrast, the antigorite crystals that abut the slip zone were  
161 mainly decomposed, without distinct cracks or fibrous textures as those observed in the  
162 host rock far from the slip zone (Figs 5 and 6a–c). These textural features indicate that

163 the serpentine crystals were decomposed in a narrow zone of <3 mm width, developed  
164 each side of the slip zone, within which the serpentine was subjected to dehydration  
165 reactions during the HVF experiments (see below for details).

166 Some molten run products were extruded from the simulated fault after 0.5 sec of the  
167 onset of slip, occurring as irregular branch-like forms of <2 mm in diameter and up to 3  
168 cm in length, showing flow structure and with a vitreous luster similar to that of fresh  
169 lava (Fig. 7a). Molten material that includes numerous fine-grained clasts is generally  
170 heterogeneous in texture under the microscope, showing flow structure and containing  
171 numerous spherical to elliptical vesicles ranging in diameter from sub-micron size to 0.5  
172 mm (Figs 6d and 7b). Such vesicular structures are considered to form via the extrusion  
173 of gas (water vapor) from a melt during frictional melting, as reported previously in both  
174 natural pseudotachylyte [e.g., Maddock et al., 1987; Lin, 1994, 2008; Magloughlin,  
175 2011] and experimentally generated pseudotachylyte [Lin and Shimamoto, 1998]. These  
176 structural features observed in the present experiments indicate that molten material  
177 formed and water vapor was released from the slip zone during the HVF experiments  
178 (Fig. 4).

179 The vesicles and flow structures are observed in narrow zones of <3 mm wide  
180 bounded by antigorite crystals on each side of the slip zone (Figs 5a and 6a–c). The  
181 fibrous textures of antigorite crystals observed in the starting serpentine samples are not  
182 recognized in the dehydration zones that abut the slip zone (Figs 5b and 6a–c).

183

### 184 ***3.2. Powder X-ray Diffraction Analysis***

185



186 Two types of run products were analyzed by powder X-ray diffraction method: one is  
187 the molten material remained in the slip zone (HVF R001), and another is the molten  
188 material of run product extruded from the slip zone during the HVF experiment (HVF  
189 R012). For comparison with the run products, the host serpentinite sample and olivine  
190 mineral sample were also analyzed. Powder X-ray diffraction analyses reveal that the  
191 diffraction peaks of antigorite are absent from the spectra of the run products, even  
192 though antigorite made up ~65% of the starting samples (Fig. 8). The integrated  
193 intensities of olivine peaks in the spectra for run materials (Fig. 8c, d) are slightly  
194 stronger than those for the serpentinite sample (Fig. 8a). The diffraction spectra of both  
195 types of run products contain a distinctive, broad band ranging from  $2\theta$  values of  $12^\circ$  to  
196  $42^\circ$ , comparable with that for a standard sample containing 5–10 wt.% glass (Fig. 8d–f).  
197 These diffraction patterns are also comparable with the XRD spectra of standard  
198 samples analyzed for the quantitative calibration of glassy materials contained in the  
199 HVF experimentally generated pseudotachylyte, as reported by Lin and Shimamoto  
200 (1998). This finding indicates that up to 10 wt.% glass or amorphous material formed in  
201 the run products that were extruded and remained in the slip zone during the present  
202 experiments, as observed under optical and electron microscopes (Figs 5 and 6).

203

### 204 ***3.3. Chemical Compositions***

205

206 The bulk chemical composition of serpentinite samples used in the frictional  
207 experiments was analyzed by X-ray fluorescence (XRF) (sample Host1 in Table 2). For  
208 comparison with the run products, the chemical composition of serpentine and olivine

209 minerals in samples of host rock (samples HS1-HS5 and HO1-2 in Table 2) was  
210 measured using an electron-probe microanalyzer (EPMA, JXA733). The chemical  
211 compositions of run products in the slip zone and in the dehydration zones (Fig. 5) were  
212 measured from a thin section oriented perpendicular to the slip zone, as shown in Fig. 3c  
213 (Tables 3–4).

214 The molten materials derived from the slip zone are generally heterogeneous in  
215 chemical composition (Fig. 9, Table 3), which differs from the bulk composition of the  
216 host rock, and from that of serpentine and olivine minerals contained in the host rock,  
217 respectively (Fig. 9, Table 2). The serpentine minerals in the dehydration zones  
218 (samples Dh1–Dh8 in Table 4) have a similar composition with that of serpentine  
219 minerals in the host rock with the sum of elements of 2.82-2.84 (Fig. 9, samples  
220 HS1–HS6, in Table 2). The variation diagrams of major oxides show a characteristic  
221 change in SiO<sub>2</sub>, MgO, FeO, CaO and Al<sub>2</sub>O<sub>3</sub> components in the run products (Fig. 9).  
222 Comparing with the dehydration zones, the molten materials in the slip zone have lower  
223 SiO<sub>2</sub> and Al<sub>2</sub>O<sub>3</sub> components and higher FeO component similar to that of olivine  
224 minerals contained in the host rock (Fig. 9). The slip zone has a large variation range in  
225 CaO and FeO components which are generally higher than that of serpentine minerals  
226 contained in the host serpentinite. There is also a large variation range in MgO  
227 component of the molten materials. In contrast, there is a small variation range in MgO  
228 component in serpentine minerals contained in the host serpentinite and dehydration  
229 zone (Fig. 9). The variations of chemical composition in the molten materials may be  
230 caused by friction melting of serpentine and olivine minerals, in which molten materials  
231 were not completely mixed and contaminated.

232 The analytical totals of the molten materials in the slip zone and serpentine minerals  
233 that abut the slip zone are up to >97.6–99.6 wt.% (Tables 3–4), higher than that of  
234 serpentine minerals in the host rock (samples HS1–HS6 in Table 2). These high total  
235 amounts can be interpreted as a result of water release from the slip zone and bounding  
236 zones due to the dehydration of serpentine minerals (see below for details).

237

### 238 ***3.4. Frictional Coefficient and Shortening Amount***

239

240 The frictional coefficient  $\mu$  showed an immediate increase to 0.56 at the onset of slip,  
241 within the first 0.1 sec of the experiments, but just as quickly dropped to a steady-state  
242 value of 0.23 prior to an elapsed time of 0.2 sec during the HVF experiments (Fig.  
243 10a–b). This pronounced peak in friction accompanied the outspray of water vapor and  
244 axial shortening of the sample within the first 0.2 sec of each run. In contrast to the HVF  
245 experiments, during the LVF experiments the frictional coefficient  $\mu$  increased to 0.57  
246 within a 2.5-sec period after 1 sec of the onset of slip, and gradually dropped to a  
247 steady-state value of 0.28 prior to an elapsed time of ~20 sec, without distinct axial  
248 shortening in the first 60 sec (Fig. 10c–d). This result indicates that slip weakening  
249 occurred over a shorter period during the HVF experiments compared with the LVF  
250 experiments.

251 During the HVF experiment, axial shortening occurred in the first 0.5 sec, and the  
252 shortening amount decreased slightly from 0.025 to 0.02 mm over a period of 4.5 sec,  
253 which corresponds to the onset of extrusion of molten run materials from the slip zone  
254 (Fig. 10b). Significant shortening occurred continuously from 5 sec after the onset of

255 high-velocity slip (Fig. 10a), which corresponds to the period of extrusion of large  
256 amount of molten run products from the slip zone (Fig. 4). In contrast, during the LVF  
257 experiments, shortening occurred after 61 sec had passed since the initiation of slip (Fig.  
258 10c–d).

259

### 260 *3.5. FTIR and TG–DSC Analyses*

261

262 To quantitatively analyze the water contents of the starting rock sample and the run  
263 products, we performed Fourier transform infrared (FTIR) and thermogravimetry  
264 (TG)–differential scanning calorimetry (DSC) spectroscopic analyses using Jasco  
265 FT/IR-300E and Netzsch STA 449C Jupiter apparatuses, respectively.

266 The run products of three HVF experiments (slip rate of 1.10 m/s and normal stresses  
267 of 2, 5, and 9 MPa, respectively) were selected for FTIR analysis, which was performed  
268 along profiles across the slip zone in thin sections of ~0.25 mm thick. In the FTIR  
269 spectra, absorption bands are observed at the OH stretching region ( $3500\text{--}3700\text{ cm}^{-1}$ ) in  
270 the host serpentine sample but not in the slip zone ('run product' in Fig. 11). This result  
271 indicates that little water (OH) remained in the slip zone. The water contents were  
272 calculated using OH peaks at  $3500\text{--}3700\text{ cm}^{-1}$  based on the method proposed by Beran  
273 and Libowitzky [2006]. The calculated water contents are shown in Fig. 12.

274 The FTIR analyses show that no water occurs in the slip zone or in the adjacent  
275 dehydration zones, and the water content ranges from 0.5 to 15 wt.% in the host rocks  
276 (Fig. 12). These results indicate that all of the water in the slip zone and adjacent  
277 dehydration zones (see Fig. 11) was released during the HVF experiments.

278 Four run products, of two HVF (1.10 m/s, No.1 and No.3) and two LVF (0.35 m/s,  
279 MH001) experiments performed under normal stresses of 2.4–2.5 MPa, were powdered  
280 for TG–DSC analysis. For comparison, one sample of host rock was also analyzed.  
281 Approximately 30 mg of sample was placed in a covered Pt<sub>90</sub>Rh<sub>10</sub> crucible and heated  
282 from 25°C to 1050°C at a rate of 10°C min<sup>-1</sup> under a flow of nitrogen gas (50 ml min<sup>-1</sup>).

283 The DSC–TG spectra of the host rock sample reveal (i) a weight loss after heating of  
284 6.9 wt.%, as determined by TG (Fig. 13a); and (ii) the heat flux during heating showed  
285 an endothermic peak at 550–700°C and an exothermic peak at 800–850°C (Fig. 13b).  
286 The first peak was accompanied by a weight loss, indicating that it corresponds to a  
287 dehydroxylation reaction. The second peak was not accompanied by a weight loss, and  
288 its relation to the reactions is currently unknown. The host sample was heated a second  
289 time, from 25°C to 1050°C, showing no weight loss and no endothermic peak,  
290 confirming that the dehydroxylation was completed during the first heating. The EPMA  
291 analyses indicate marked differences in the analytical totals among the serpentine  
292 minerals of the host rock (Table 2), the molten material remaining in the slip zone  
293 (Table 3), and the dehydration zones (Table 4). The totals for the molten materials and  
294 dehydration zones that abut the slip zone are up to 97–99.5 wt.%, about 9–11 wt.%  
295 higher than that of the serpentine minerals of the host rock. Considering the presence of  
296 ~35% olivine in the host rock sample, the differential amounts of 9–11 wt.% are  
297 comparable to the weight loss of 6.9 wt.% in the run products, including molten  
298 materials and fine-grained clasts of the host rock, as determined by TG (Fig. 13a).  
299 Accordingly, the difference in analytical total reflects the release of water from the  
300 molten materials and from serpentine minerals that abut the slip zone, due to the

301 dehydration of serpentine minerals.

302 Figure 13 shows the TG –DSC spectra of four run products, revealing that the total  
303 weight losses of water are 0.0 wt.% for samples No. 1 and No. 3, 7.3 wt.% for MH001,  
304 and 4.3 wt.% for MH002 (Fig. 14a). Samples No. 1 and No. 3 show no significant  
305 endothermic peak at around 550–700°C (Fig. 14b), indicating that the dehydroxylation  
306 reaction was completed in the HVF samples. In contrast, MH001 and MH002 show a  
307 weight loss and an endothermic peak at around 550–700°C (Fig. 14b), similarly to the  
308 host rock (Fig. 13b). This result suggests that the dehydroxylation reaction was not  
309 completed during the LVF friction experiment at a low velocity of 0.35 m/s.

310

#### 311 **4. Discussion and Conclusions**

312

##### 313 ***4.1. Coseismic Melting and Dehydration Reaction***

314

315 The ejection of water vapor and the generation of vesicles within run products during  
316 the HVF experiments provide conclusive proof that water was released from the slip  
317 zone. The flow structures, the vitreous luster of run products (similarly to that of fresh  
318 lava), and X-ray diffraction patterns indicate the coexistence of abundant fluid derived  
319 from serpentine and frictional melt resulting from frictional heating in the slip zone. The  
320 absence of antigorite crystals in the X-ray diffraction spectra of run products can be  
321 interpreted as a result that antigorite crystals were completely broken down and/or  
322 melted by friction heating.

323 As shown in Fig. 9, the molten materials have lower SiO<sub>2</sub> and Al<sub>2</sub>O<sub>3</sub> components and

324 higher FeO component similar to that of olivine mineral contained in the host rock than  
325 that of serpentine mineral in the dehydration zone, and higher CaO and FeO components  
326 than that of serpentine contained in the host serpentinite. The FeO component of the  
327 molten materials is about 5~7 wt% higher than that of serpentine minerals contained in  
328 the host serpentinite and the dehydration zones, which is similar to that of olivine  
329 mineral contained in the host rock (Fig. 9). Furthermore, MgO and Al<sub>2</sub>O<sub>3</sub> components of  
330 the molten materials are locally similar to that of olivine mineral, higher than that of the host  
331 serpentine minerals contained in the host serpentinite and the dehydration zones (Fig. 9).  
332 These textural and petrologic features including the chemical compositions of molten  
333 materials reveal that not only the serpentine but also the olivine minerals were  
334 melted by friction heating, and that a high temperature reached the bounding zones of  
335 the slip zone at which serpentine was involved in a dehydration reaction. Previous  
336 studies show that the high-velocity friction melting occurs in a chemically  
337 non-equilibrium process (Lin and Shimamoto, 1998; Lin, 2008) and that the melting or  
338 breakdown of serpentine mineral occurs at temperature of 400~600 °C [Spray, 1992].  
339 Thus, the serpentine and olivine minerals are considered to be melted at temperature of  
340  $\geq$  melting points of these minerals. Based on the melting point (~1890 °C) of olivine  
341 [Spray, 1992], it is estimated that the temperature in the slip zone reached at least up to  
342 1890 °C during the HVF experiments.

343 Previous studies indicate that the dehydration of serpentine occurs at temperature of  
344  $\geq 500^{\circ}\text{C}$  [Ulmer and Trommsdorff, 1995; Viti, 2010] to  $856^{\circ}\text{C}$  [Lange and Ahrens,  
345 1982]. In previous HVF experiments using marble samples, direct thermometer-based  
346 measurements of temperature indicate that the slip-zone temperature can reach

347 600–900°C during the first 0.1 sec of the experiment at a slip rate of 1.17 m/s [Han et al.,  
348 2007]. TG, DTG and differential thermal analyzer (DTA) analyses show that serpentine  
349 dehydration takes place between 550 and 800°C [Viti, 2010]. Calculation results for an  
350 HVF experiment on serpentinite at a slip rate of 1.1 m/s reveal that the flash temperature  
351 can rise by ~1250°C over a period of <0.1 sec [Hirose and Bystricky, 2007] and that the  
352 temperature can reach 550–1100°C within a narrow slip zone (<3 mm wide) over a  
353 period of 2–3 sec [Fukuchi and Imai, 2001]. Furthermore, seismic data reveal that if the  
354 shear energy is constrained within 1 cm of the slip plane during seismic slip, the  
355 temperature can readily increase to 100–1000°C during a medium- to large-magnitude  
356 earthquake [Kanamori and Brodsky, 2004]. Thus, the temperature up to 1890°C in the  
357 present HVF experiments as documented above, within a dehydration zone of <2 mm in  
358 width (Fig. 12) and at slip rates of 1.10–1.31 m/s, is sufficient to induce the dehydration  
359 of serpentine.

360 The breakdown of serpentine to olivine + talc + water and the breakdown of talc to  
361 enstatite + quartz + water at 1 bar follow a second-order rate law [Bose and Ganguly,  
362 1994]. The breakdown of antigorite in the present experiments is indicated by the  
363 consumption of antigorite and increased integrated intensities of olivine in the X-ray  
364 diffraction spectra for the run products, although talc could not be identified from the  
365 spectra. Direct observations made during the present experiments also demonstrate that  
366 serpentine dehydration reaction occurred within 0.2 sec of the onset of slip. Furthermore,  
367 the antigorite crystals observed in the dehydration zones that abut the slip zone show  
368 textural features indicative of decomposition, without the distinct cracks and fibrous  
369 texture observed in the starting sample of host rock (Figs 5 and 6a–c). This finding



370 demonstrates that the serpentine dehydration reaction that occurred in a wide zone  
371 involving the slip zone was caused mainly by the diffusion of frictional heat from the  
372 slip zone. Our results support the idea that the diffusion of frictional heat is a major  
373 coupling factor of thermal pressurization caused by the dehydration of serpentine within  
374 seismogenic fault zone [Brantut et al., 2010].

375

#### 376 ***4.2. Mechanism of Dynamic Weakening***

377

378 The dynamic weakening of faults during earthquakes is considered to result from  
379 several mechanisms, including friction melting [Spray, 1993; Hirose and Shimamoto,  
380 2005; Di Toro et al., 2006, 2011], the presence of S–C cataclasites [Lin, 1999, 2008],  
381 the formation of fault gouge [e.g., Rice, 2006; Mizoguchi et al., 2007], thermal  
382 pressurization [e.g., Lachenbruch and Sass, 1980; Wibberley and Shimamoto, 2005],  
383 dehydration reactions involving water-rich minerals such as serpentine and kaolinite  
384 [e.g., Hirose and Bystricky, 2007; Brantut et al., 2008; Viti and Hirose, 2010; Kohli et  
385 al., 2011] as well as fault gouges present in seismogenic fault zones [e.g., Famin et al.,  
386 2008; Hamada et al., 2009, 2011], thermal decomposition [Han et al., 2007], and the  
387 dehydroxylation of mica minerals [Hirono and Tanikawa, 2011]. Each of these  
388 mechanisms is closely linked to frictional heating generated upon the fault plane during  
389 seismic slip. The frictional melt generated in the slip zone also plays an important role  
390 in lubricating the slip plane, thereby facilitating further slip along seismogenic faults  
391 during large earthquakes [e.g., Di Toro et al., 2006, 2011]. Although dynamic fault  
392 strength during frictional melting is commonly considered to be controlled by the

393 development of a molten layer and by the viscosity of this layer [Spray, 1993; Hirose  
394 and Shimamoto, 2005], the serpentinite dehydration may also be a main mechanism  
395 resulting in a dramatic increase in pore pressure that may lead to the dynamic weakening  
396 of seismogenic faults. The outspray of water vapor within the first 0.2 sec of each run as  
397 observed during the HVF experiments indicates that the dehydration of serpentine  
398 occurred in the first 0.2 sec. The fact that molten materials were squeezed out after 0.5  
399 sec after the onset of the slip from the slip zone as observed during the experiments  
400 reveals that a molten layer was produced in the same time as the water vapor within the  
401 slip zone during the first 0.5 sec. These findings indicate that both water vapor and  
402 molten material were co-existed in the slip zone in the first 0.5 sec of the run. It may be  
403 difficult to produce sufficient fault gouge material to affect the fault strength over a  
404 short duration of 0.2 sec because of small amount of generated slip. Accordingly, the  
405 dramatic decrease in the frictional coefficient from 0.56 to 0.25 in the first 0.2 sec after  
406 the onset of slip (Fig. 10a–b) can be interpreted as a result of thermal pressurization  
407 caused by the dehydration of serpentine that accompanies frictional melting during the  
408 HVF experiments. In contrast, similar weakening was observed in the LVF experiments,  
409 in which the frictional coefficient decreased from 0.55 to 0.25, but this took ~10 sec  
410 after the onset of run (Fig. 10c–d). This may be interpreted as that enough amount of  
411 fine-grained material (fault gouge) formed in the slip zone which weakened the fault  
412 strength as proposed by previous studies [Rice, 2006; Mizoguchi et al., 2007].

413 In the present study, it is considered that the main weakening mechanism of the  
414 simulated faults under conditions equivalent to large earthquake slip was the thermal  
415 pressurization caused by serpentine dehydration associated with frictional heating and

416 melting, resulting in the excess saturation pressure of water vapor and fluid including  
417 melt in the slip zone. Previous studies show that frictional heating would cause the fluid  
418 in the fault gouge to expand in volume much more than would be the solid cage [e.g.,  
419 Sibson, 1973, Lachenbruch and Sass, 1980]. Thus, shear-induced dilatancy of the gouge  
420 overwhelms the thermal expansion effect and a pressure increase must be induced in  
421 the pore pressure [Rice and Cocco, 2007]. The saturation pressure of water vapor is  
422 known to vary with the temperature of the vapor [Kaye and Laby, 1986]: when confined  
423 water is heated, the saturation pressure of water vapor (P) shows a rapid increase.  
424 Assuming ideal gas (water vapor) behavior,  $P = nRT/V$ , where n is the number of moles,  
425 R is the water vapor constant, T is absolute temperature (K), and V is the volume of  
426 water vapor. From room temperature (20°C) to 360°C, P increases by three orders of  
427 magnitude, from  $\sim 10^{-2}$  to  $\sim 20$  MPa [Kaye and Laby, 1986]. Theoretically, under the  
428 pressure–temperature conditions of seismogenic depths, the thermal expansivity of  
429 water is on the order of  $10^{-3}/^{\circ}\text{C}$ , meaning that the increase in fluid pressure at the depths  
430 of hypocenters would be on the order of 1 MPa/ $^{\circ}\text{C}$  [Lachenbruch and Sass, 1980;  
431 Kanamori and Brodsky, 2004]. Thus, the corresponding pressure of water vapor and  
432 fluid would be  $>20$  MPa in a simulated fault zone under conditions equivalent to large  
433 earthquake slip, comparable to the stress drop that occurs during large earthquakes  
434 [O'Hara et al., 2006]. In the present HVF experiments, the decrease in the average  
435 shortening amount in the first 5 sec after the onset of slip can be interpreted as a result  
436 of pore pressure increase due to the thermal pressurization that accompanies frictional  
437 melting within the slip zone. The subsequent increase in the average shortening amount  
438 could reflect the extrusion of run products (including vapor, melt, and fine-grained

439 materials) from the slip zone, as shown in Fig. 4.

440 Our results support the idea that the thermal pressurization of fluid released by the  
441 dehydration of serpentine and friction melt plays an important role in the dynamic  
442 weakening of faults during seismic slip within seismogenic fault zones.

443

#### 444 ***4.3. Tectonic Implications***

445

446 The present experimental results have significant implications for subduction zone  
447 earthquakes and transform faults such as the San Andreas Fault. Seismogenic faults  
448 within a subduction zone are generally associated with a mantle wedge composed of  
449 serpentinites that contain ~13 wt.% H<sub>2</sub>O [Ulmer and Trommsdorff, 1995]. Hydrous  
450 antigorite may play an important role in the transport of water into the earth when it  
451 enters a subduction zone. The present results show that the frictional heat generated  
452 upon a seismogenic slip plane under conditions of large earthquake slip can lead to  
453 melting in a seismic slip zone and the dehydration of serpentinite within a wide  
454 dehydration reaction zone (comprising the main slip zone and bounding zones) due to  
455 the diffusion of frictional heat from the slip plane, thereby increasing the pore pressure  
456 due to the thermal expansivity of fluid and water vapor. Furthermore, the frictional melt  
457 generated in the slip zone also plays an important role in lubricating the slip plane,  
458 facilitating further slip along seismogenic faults during large earthquakes (Di Toro et al.,  
459 2011). Accordingly, our experiment results confirm that the serpentine dehydration that  
460 accompanies frictional melting results in a sudden increase in pore pressure, which in  
461 turn may lead to a reduction in the effective normal stress across the fault, in turn

462 resulting in a marked reduction in the dynamic fault strength, thereby enabling further  
463 slip along the fault in a subduction zone.

464 This sequence of events might also influence the physics of earthquake processes  
465 within subduction zones, explaining the large seismic slip of >15–50 m generated by  
466 huge subduction-zone earthquakes such as the 2004  $M_w$  9.4 Sumatra–Andaman  
467 earthquake [Subarya et al., 2006] and the 2011  $M_w$  9.1 Tohoku Japan earthquake [Yagi  
468 and Fukahata, 2011]. In addition, if the large volumes of fluid released by the  
469 dehydration of serpentinites during huge earthquakes are concentrated upon and migrate  
470 along pre-existing fault zones to neighboring fault segments, such a sudden increase in  
471 fluid pressure would promote further brittle failure in barrier areas of seismogenic faults  
472 and in neighboring fault segments. The present results indicate that the dynamic  
473 parameters of seismogenic faults are strongly affected by serpentine dehydration during  
474 large earthquakes within subduction zones and along intracontinental faults that contain  
475 abundant hydrous minerals.

476

#### 477 **Acknowledgments**

478

479 We are grateful to Prof. T. Shimamoto for designing the rotary-shear low- to  
480 high-velocity test machine. This work was supported by a Grand-in-Aid for Scientific  
481 Research (Science Project No. 23253002 for A. Lin) from the Ministry of Education,  
482 Culture, Sports, Science and Technology of Japan.

483

484 **References**

485

486 Andrews, D. J., 2002. A fault constitutive relation accounting for thermal pressurization  
487 of pore fluid. *J. Geophys. Res.* 107, B001942, doi:10.1029/2002J.

488 Beran, A., Libowitzky, E., 2006. Water in natural mantle minerals II: olivine, garnet  
489 and accessory minerals. *Reviews in Mineralogy and Geochemistry*, 62, 169–191.

490 Bose, K., Ganguly, J., 1994. Thermogravimetric study of dehydration kinetics of talc.  
491 *Am. Mineral.* 79, 692-699.

492 Brantut, N., Schubnel, A., Rouzaud, J.-N., Brunet, F., Shimamoto, T., 2008. High  
493 velocity frictional properties of a clay-bearing fault gouge and implications for  
494 earthquake mechanics. *J. Geophys. Res.* 113, B10401, doi:10.1029/2007JB005551.

495 Brantut N., Schubnel, A., Corvisier, J., Sarout, J., 2010. Thermochemical pressurization  
496 of faults during coseismic slip. *J. Geophys. Res.* 115, B05314,  
497 doi:10.1029/2009JB006533.

498 Brantut, N., Han, R., Shimamoto, T., Findling, N., Schubnel, A., 2011. Fast slip with  
499 inhibited temperature rise due to mineral dehydration: Evidence from experiments  
500 on gypsum. *Geology* 39, 59–62.

501 Christensen, N. J., 1972. The abundance of serpentinites in the oceanic crust. *J. Geophys.*  
502 *Res.* 80, 709–719.

503 Di Toro, G., Goldsby, D. L., Tullis, T. E., 2006. Friction falls towards zero in quartz  
504 rock as slip velocity approaches seismic rates. *Nature* 427, 436–439.

505 Di Toro, G., Han, R., Hirose, T., De Paola, N., Nielsen, S., Mizoguchi, K., Ferri, F.,  
506 Cocco, M., Shimamoto, T., 2011. Fault lubrication during earthquakes, *Nature*, 471,

507 494-498.

508 Famin, V., Nakashima, S., Boullier, A.-M., Fujimoto, K., Hirono, T., 2008. Earthquake  
509 produce carbon dioxide in crustal faults. *Earth and Planetary Sci. Lett.* 265,  
510 487–497.

511 Francis, T. J. G., 1981. Serpentinization faults and their role in the tectonics of slow  
512 spreading ridges. *J. Geophys. Res.* 86, 11616-11622.

513 Fukuchi, T., Imai, N., 2001. ESR and ICP analyses of the DPRI 500 m drill core  
514 samples penetrating through the Nojima Fault, Japan. *Island Arc* 10, 465– 478.

515 Goldsby, D.L., Tullis, T., 2011. Flash heating leads to low frictional strength of crustal  
516 rocks at earthquake slip rates. *Science* 334, 216–218.

517 Hamada, Y., Hirono, T., Tanikawa, W., Soh, W., Song, S., 2009. Energy taken up by  
518 co-seismic chemical reactions during a large earthquake: An example from the  
519 1999 Taiwan Chi-Chi earthquake. *Geophys. Res. Lett.* 36, L06301,  
520 doi:10.1029/2008GL036772.

521 Hamada, Y., Hirono, T., Ishikawa, T., 2011. Coseismic frictional heating and fluid-rock  
522 interaction in a slip zone within a shallow accretionary prism and implications for  
523 earthquake slip behavior. *J. Geophys. Res.* 116, B01302,  
524 doi:10.1029/2010JB007730.

525 Han, R., Shimamoto, T., Hirose, T., Ree, J.-H., Ando J., 2007. Ultra-low friction of  
526 carbonate fault caused by thermal decomposition. *Science* 316, 878–881.

527 Han, R., T. Hirose, Shimamoto, T., 2010. Strong velocity weakening and powder  
528 lubrication of simulated carbonate faults at seismic slip rates. *J. Geophys. Res.* 115,  
529 B03412, doi:10.1029/2008JB006136.

530 Hirono, T., Tanikawa, W., 2011. Implications of the thermal properties and kinetic  
531 parameters of dehydroxylation of mica minerals for fault weakening, frictional  
532 heating, and earthquake energetics. *Earth and Planetary Sci. Lett.* 307, 161–172.

533 Hirono, T., Fujimoto, K., Yokohama, K., Hamada, T., Tanikawa, W., Tadai, O.,  
534 Mishima, T., Tanimizu, M., Lin, W., Soh, W., Song, S., 2008. Clay mineral  
535 reactions caused by frictional heating during an earthquake: An example from the  
536 Taiwan Chelungpu fault. *Geophys. Res. Lett.*, 35, L16303,  
537 doi:10.1029/2008GL034476.

538 Hirose, T., Shimamoto, T., 2005. Growth of molten zone as a mechanism of slip  
539 weakening of simulated faults in gabbro during frictional melting. *J. Geophys. Res.*  
540 110, B05202, doi:10.1029/2004JB003207.

541 Hirose, T., Bystricky, M., 2007. Extreme dynamic weakening of faults during  
542 dehydration by coseismic shear heating. *Geophys. Res. Lett.* 34, L14311,  
543 doi:10.1029/2007GL030049.

544 Kanamori, H., Brodsky, E. E., 2004. The physics of earthquake, *Rep. Prog. Phys.* 67,  
545 1429–2496.

546 Kaye, G.W.C., Laby, T. H., 1986. *Tables of physical and chemical constants.* John  
547 Willey and Sons Inc., New York, 432p.

548 Kohli, A.H., Goldsby, D. L., Hirth, G., Tullis, T., 2011. Flash weakening of serpentinite  
549 at near-seismic slip rates. *J. Geophys. Res.* 116, B03202,  
550 doi:10.1029/2010JB007833

551 Lachenbruch, A. H., and J. H. Sass (1980), Frictional heating, fluid pressure, and the  
552 resistance to fluid motion. *J. Geophys. Res.*, 85, 6185–6222.



- 553 Lange, M. A., Ahrens, T. J., 1982. Impact induced dehydration of serpentine and the  
554 evolution of planetary atmospheres, *J. Geophys. Res.* 87, A451–A456.
- 555 Lin, A., 1994. Glassy pseudotachylyte veins from the Fuyun fault zone, northwest China.  
556 *J. Struct. Geol.* 16, 71–83.
- 557 Lin, A., 1999. S-C cataclasite in granitic rocks. *Tectonophysics* 304, 257–273.
- 558 Lin, A., 2002. Co-seismic strike-slip and rupture length produced by the Ms 8.1 Central  
559 Kunlun earthquake. *Science* 296, 2015–2017.
- 560 Lin, A., 2008. Fossil earthquakes: the formation and preservation of pseudotachylytes.  
561 Springer, Berlin, 348p.
- 562 Lin, A., Shimamoto, T., 1998. Selective melting processes as inferred from  
563 experimentally-generated pseudotachylytes, *J. Asian Earth Sci.* 16, 533–545.
- 564 Maddock, R. H., Grocott, J., Van Nes, J., 1987. Vesicles, amygdales and similar  
565 structures in fault-generated pseudotachylytes. *Lithos* 20, 419–432.
- 566 Magloughlin, J. F., 2011. Bubble collapse structure: a microstructural record of fluids,  
567 bubble formation and collapse, and mineralization in pseudotachylyte. *Journal of*  
568 *Geology* 119, 351–371.
- 569 Meade, C., Jeanloz, R., 1991. Deep focus earthquake and recycling of water into the  
570 Earth's mantle. *Science* 252, 68–72.
- 571 Mizoguchi, K., Hirose, T. Shimamoto, T., Fukuyama, F., 2007. Reconstruction of  
572 seismic faulting by high-velocity friction experiments: An example of the 1995  
573 Kobe earthquake. *Geophys. Res. Lett.* 34, L01308, doi: 10.1029/2006GL027931.
- 574 Moore, D. E., Rymer, M.J., 2007. Talc-bearing serpentinite and the creeping section of  
575 the San Andreas fault. *Nature* 448, 795–797.

576 O'Hara, K. D., Mizoguchi, K., Shimamoto, T., Hower, J., 2006. Experimental frictional  
577 heating of coal gouge at seismic slip rates: Evidence for devolatilization and  
578 thermal pressurization of gouge fluids. *Tectonophysics* 424, 109–118.

579 Rice, J. R., 2006. Heating and weakening of faults during earthquake slip. *J. Geophys.*  
580 *Res.* 110, B05311, doi: 10.1029/2005J B004006.

581 Shimamoto, T., Tsutsumi, A., 1994. A new rotary-shear high-speed frictional testing  
582 machine: its basic design and scope of research. *Structural Geology, The Journal of*  
583 *Tectonic Group Japan* 39, 65–78 (in Japanese with English abstract).

584 Sibson, R., 1973. Interactions between temperature and pore-fluid pressure during  
585 earthquake faulting and a mechanism for partial or total stress relief. *Nature* 243,  
586 66–68.

587 Spray, J., 1992. A physical basis for the frictional melting of some rock-forming  
588 minerals. *Tectonophysics* 204, 2205–221.

589 Spray, J., 1993. Viscosity determination of some fractionally generated silicate melts:  
590 implication for fault zone rheology at high strain rates. *J. Geophys. Res.* 98,  
591 8053–8068.

592 Subarya, C., Chlieh, M., Prawirodirdjo, L., Avouac, J., Bock, Y., Sieh, K., Meltzner,  
593 A.J., Natawidjaja, D.H., R. McCaffrey, R., 2006. Plate-boundary deformation  
594 associated with the great Sumatra-Andaman earthquake. *Nature* 440, 46–51.

595 Tibi, R., G. Rock, Estabrook, C.H., 2002. Seismic body wave constraint on mechanisms  
596 of intermediate-depth earthquakes. *J. Geophys. Res.* 107,  
597 doi:10.1029/200JB000361.

598 Ulmer, P., Trommsdorff, V., 1995. Serpentine stability to mantle depths and

599 subduction-related magmatism. *Science* 268, 858–861.

600 Viti, C., 2010. Serpentine minerals discrimination by thermal analysis. *American*  
601 *Mineralogist* 95, 631–638.

602 Viti, C., Hirose, T., 2010. Thermal decomposition of serpentine during coseismic  
603 faulting: Nanostructures and mineral reactions. *J. Struct. Geol.* 32, 1476-1484.

604 Wibberley, C. A. J., 2007. Seismology: Talc at fault. *Nature* 448, 756–757.

605 Wibberley, C. A. J., Shimamoto, T., 2005. Earthquake slip weakening and asperities  
606 explained by thermal pressurization. *Nature* 436, 689–692.

607 Yagi, Y., Fukahata, Y., 2011. Rupture process of the 2011 Tohoku-oki earthquake and  
608 absolute elastic strain release. *Geophys. Res. Lett.* 38, L19307,  
609 doi:10.1029/2011GL048701.

610

611 **Captions to figures**

612 Figure 1. Diagram showing the rotary-shear low- to high-velocity frictional testing  
613 machine equipped with a hydraulic pressure vessel. 1: specimen holder (one-axis  
614 rotary-shear specimen box); 2: pressure vessel for elevated pore-water pressure;  
615 3–4: torque and axial force gauges; 4: electromagnetic clutch; 5: force gouge; 6:  
616 oil pressure cylinder; 7: servo-motor and gear system; 8: motor controller; 9:  
617 manual pump; 10: oil pressure pump; 11–12: manual oil pressure pump; 13:  
618 pressure generator system; 14–15: data recording system. This machine was  
619 installed at Shizuoka University, Japan, in early 2007.

620 Figure 2. Close-up view of the specimen holder (a), configuration of the specimen set (b),  
621 and orientation of the thin section cut from the run products (c). The thin section is  
622 oriented perpendicular to the slip zone.

623 Figure 3. Petrographic features of serpentinite used for the frictional experiments in this  
624 study. (a) Photomicrograph (cross polarized light); (b) scanning electron image.  
625 The serpentinite is composed of 65% serpentine (antigorite) and 35% olivine.

626 Figure 4. Photographs taken through the transparent window cover of the experimental  
627 apparatus showing dust and water vapor (a, c, d), and sparks of yellow–red melt (b)  
628 ejected from the interface (slip zone) of two cylindrical serpentinite specimens at a  
629 slip rate of 1.10 m/s and normal stress of 6.5 MPa during a high-velocity friction  
630 (HVF) experiment (HVF R001). The water vapor cooled to form water droplets  
631 (Wd) upon the window cover along a zone of 2–7 mm in width during the 20 sec  
632 duration of the experiment.

633 Figure 5. Photomicrograph (a) and back-scattered electron micrograph (b) showing

634 representative microstructures of a simulated fault zone (slip zone) in a  
635 high-velocity friction (HVF) experiment (run HVF R001) conducted at a slip rate  
636 of 1.10 m/s. Note that dehydrated zones (dz) are developed on both sides of the slip  
637 zone.

638 Figure 6. Back-scattered electron micrographs showing representative microstructures  
639 of a simulated fault zone (slip zone) in experiment run HVF R001 conducted at a  
640 slip rate of 1.10 m/s, showing (a) the slip zone and dehydration zone (dz); (b) a  
641 close-up view of the dehydrated zone in serpentine; (c) a close-up view of (b); and  
642 (d) representative textures of run products ejected from the slip zone, showing melt  
643 textures and flow layers, vesicles (v), and a fine-grained matrix (molten material).

644 Figure 7. Representative textures of run products. (a) Photograph of fine-grained matrix  
645 (molten material) ejected from the slip zone, showing flow textures, vesicles, and a  
646 vitreous luster similar to that of fresh lava. (b) Back-scattered electron micrograph  
647 showing the textures of vesicles and fine-grained clasts (HVF R001 run product).

648 Figure 8. Powder X-ray diffraction spectra derived from (a) the host serpentinite, (b)  
649 reference olivine, and (c–f) representative run products remaining in the slip zone,  
650 for experiments with a slip rate of 1.31 m/s and normal stress of 5 MPa (run HVF  
651 R012) (c), and a slip rate of 1.10 m/s and normal stress of 6.5 MPa (run HVF  
652 R001) (d). The sample (HVF 012) was picked from the run product material  
653 extruded from the slip zone, and the sample (HVF R001) was separated from the  
654 run product remained in the slip zone. (e) Enlargement of (d) between  $2\theta$  values of  
655  $15^\circ$  and  $35^\circ$ , and (f) calibrated sample containing 90 wt.% fine-grained clasts of  
656 run product and 10 wt.% glass (obsidian). ol: olivine; ant: antigorite. Note that the

657 run product (HVF R001) showed a distinct, broad range of  $2\theta$  values from  $20^\circ$  to  
658  $35^\circ$ , as observed for the calibrated sample containing 10 wt.% glass (f). The  
659 vertical axis (diffraction density) is the same for all spectra. CPS: counts per  
660 second.

661 Figure 9. Variation of major oxides in the host serpentinite, slip zone and dehydration  
662 zone generated in the HVF experiments. Data are shown in Tables 2-4.

663 Figure 10. Friction coefficient versus time for experiment run HVF R012 at a slip rate of  
664 1.31 m/s and normal stress of 5 MPa (a–b), and run LVFR110 at a slip rate of 0.35  
665 m/s and normal stress of 8 MPa (c–d). (b) Enlargement of the first 2.4 sec of the  
666 HVF experiment shown in (a). (d) Enlargement of the first 20 sec of the LVF  
667 experiment shown in (c).

668 Figure 11. Representative FTIR spectra of the host rock (serpentinite) and run product  
669 of a high-velocity friction experiment (MH R0012). Note that the OH peaks are  
670 present at  $3500\text{--}3700\text{ cm}^{-1}$  in the host serpentine sample but not in the slip zone.

671 Figure 12. Water contents of the high-velocity friction (HVF) run products calculated  
672 from the Fourier transform infrared (FTIR) spectra. Note that the narrow and wide  
673 zones reflect a change in slip zone width, as shown in Figs 5 and 6.

674 Figure 13. Thermogravimetry–differential scanning calorimetry (TG–DSC) spectra of  
675 the host rock (serpentinite). (a) TG, (b) DSC. Note that the heat flux during the  
676 heating showed an endothermic peak at  $550\text{--}700^\circ\text{C}$  and an exothermic peak at  
677  $800\text{--}850^\circ\text{C}$ .

678 Figure 14. Thermogravimetry–differential scanning calorimetry (TG–DSC) spectra of  
679 the run products of high-velocity friction (HVF) experiments (No. 1 and No. 2),

680 and low-velocity friction (LVF) experiments (MH001 and MH002). (a) TG, (b)  
681 DSC. See the text for details.  
682

Figure1  
[Click here to download high resolution image](#)

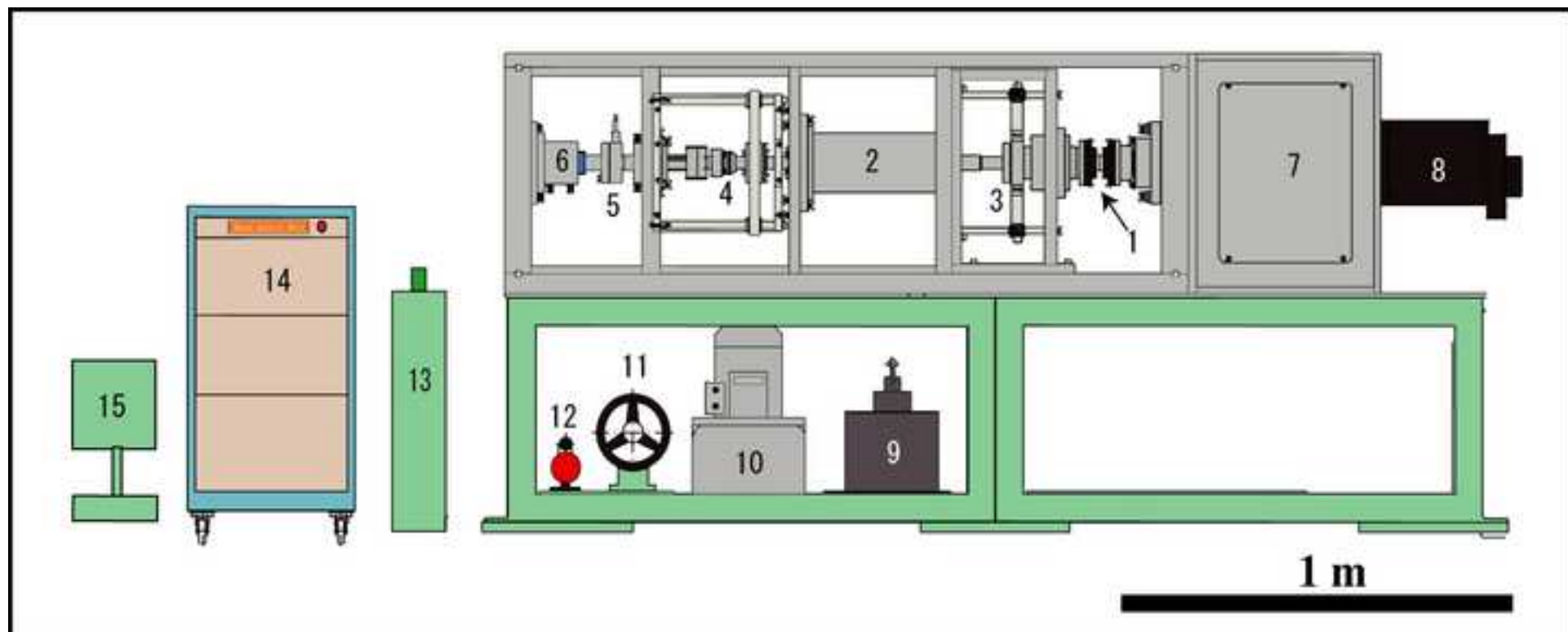




Figure2  
[Click here to download high resolution image](#)

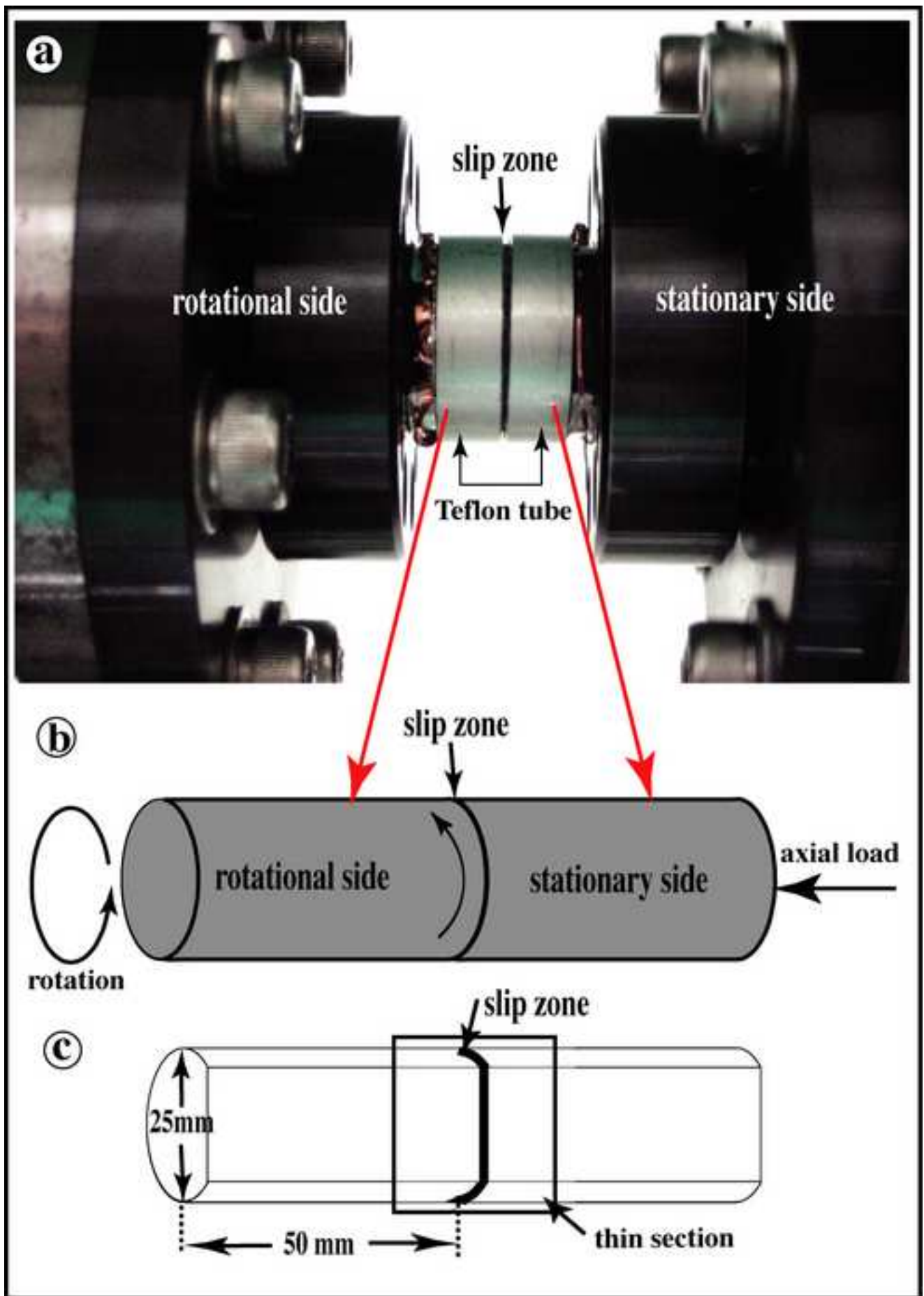


Figure3  
[Click here to download high resolution image](#)

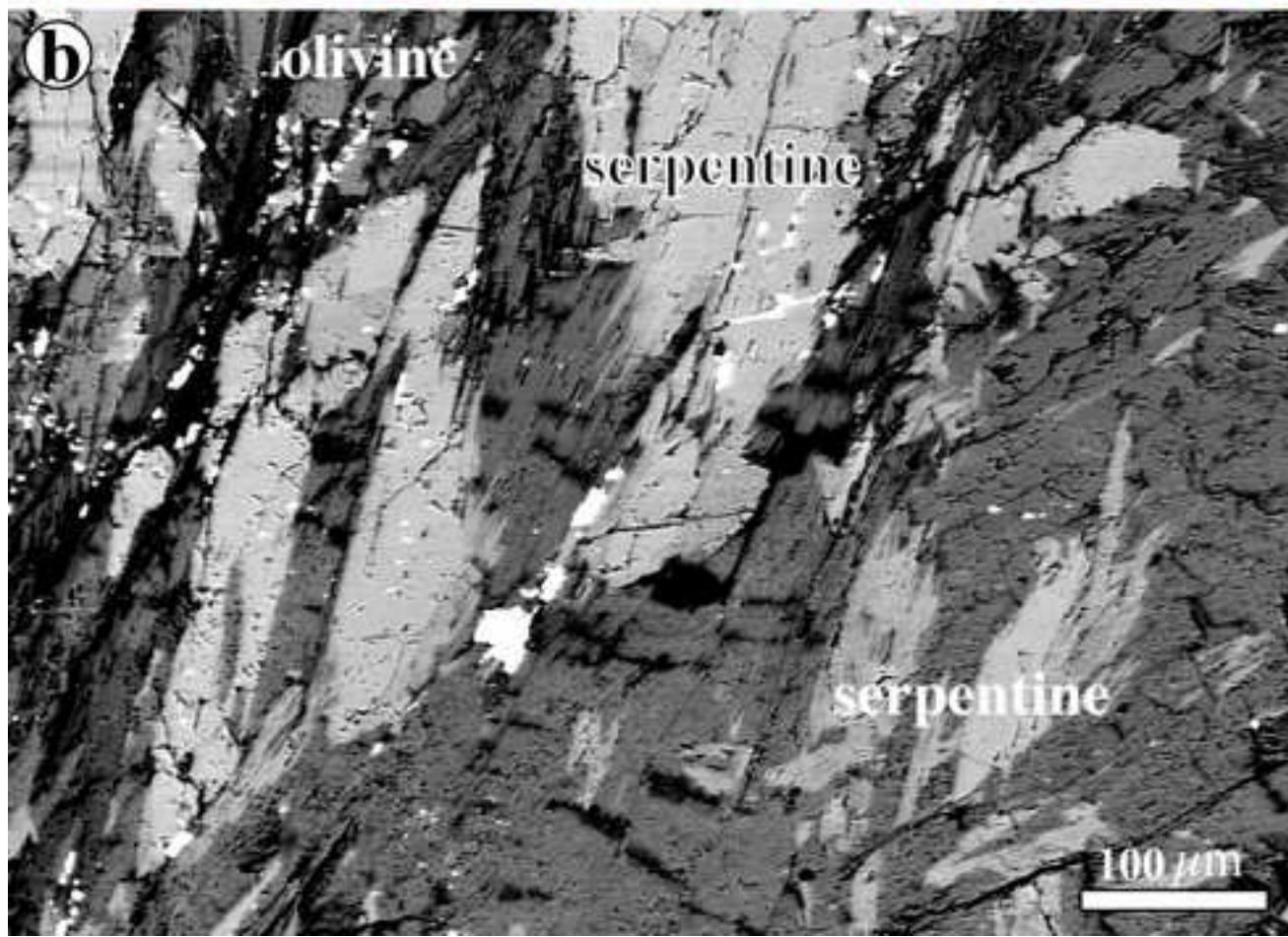
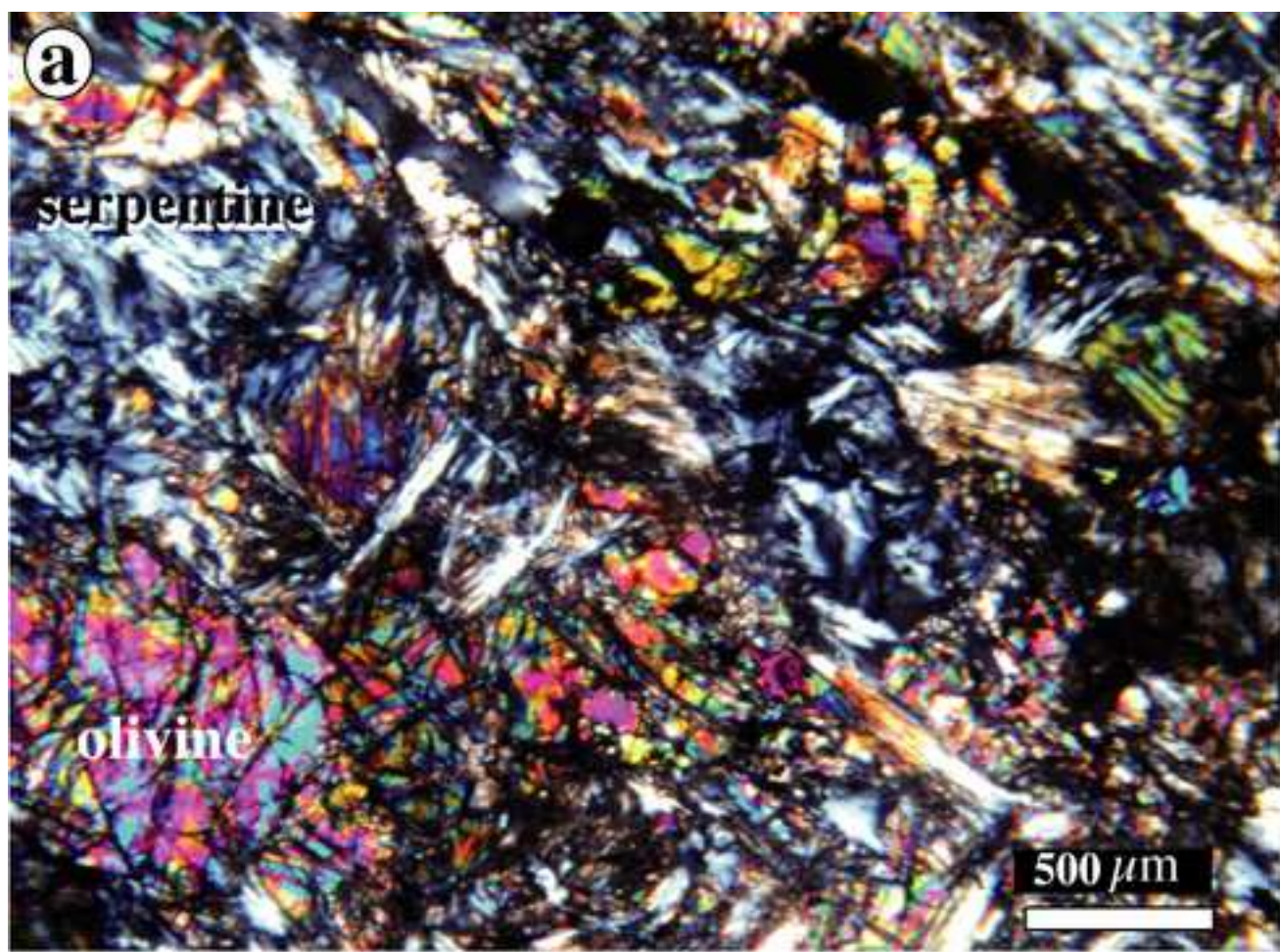


Figure4  
[Click here to download high resolution image](#)

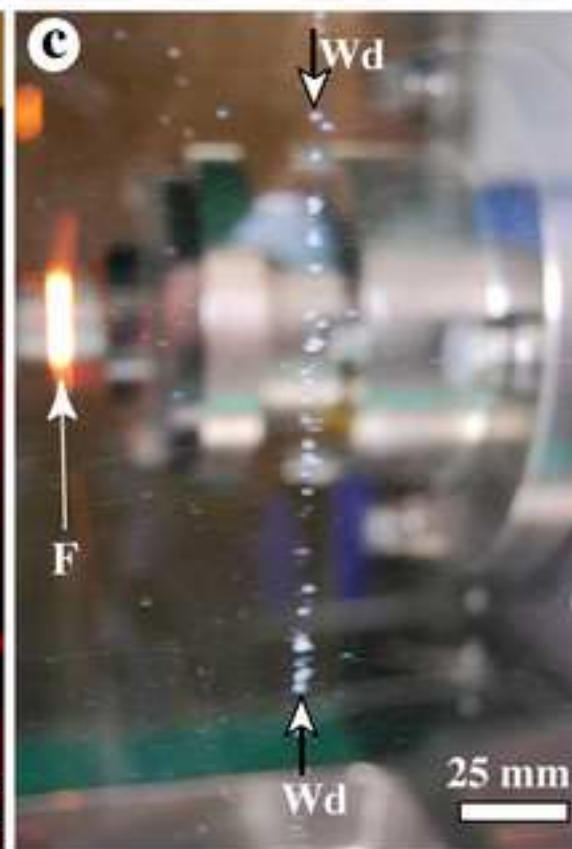
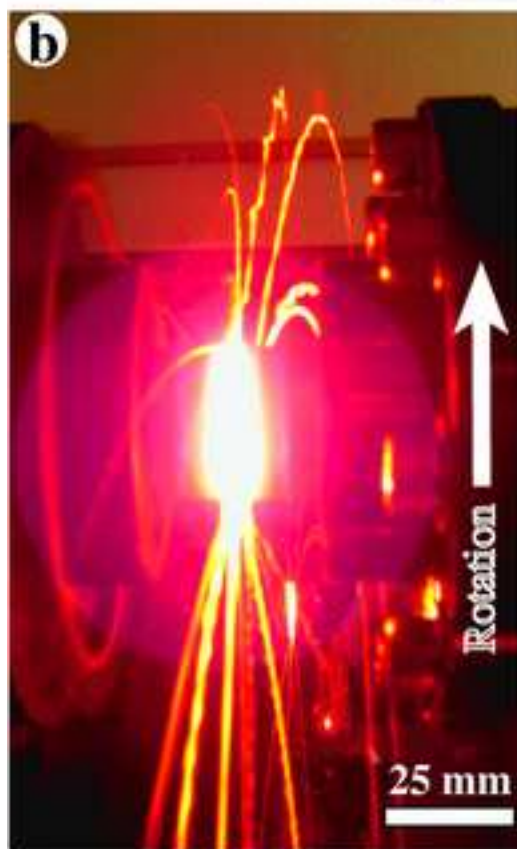
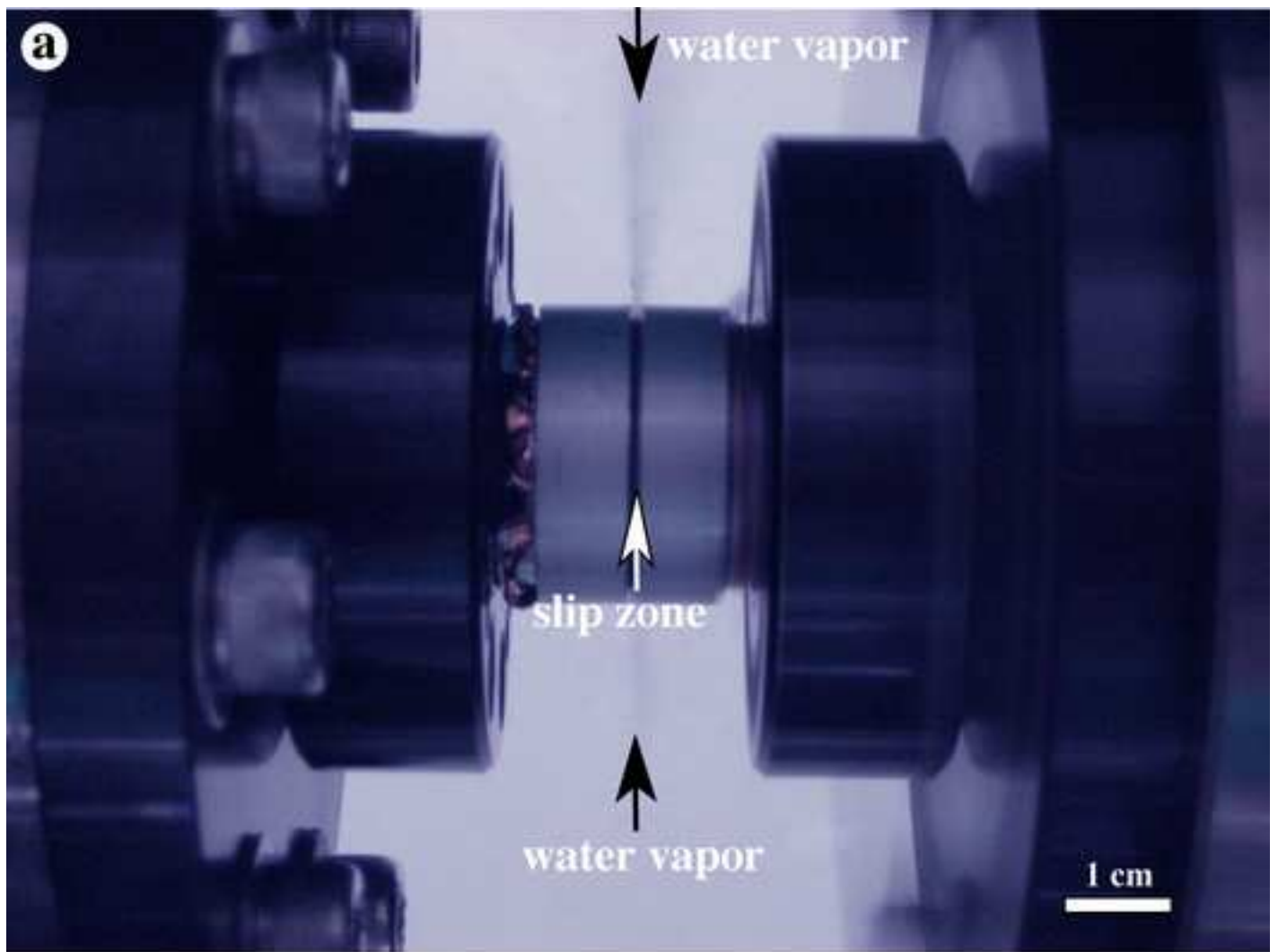


Figure 5  
[Click here to download high resolution image](#)

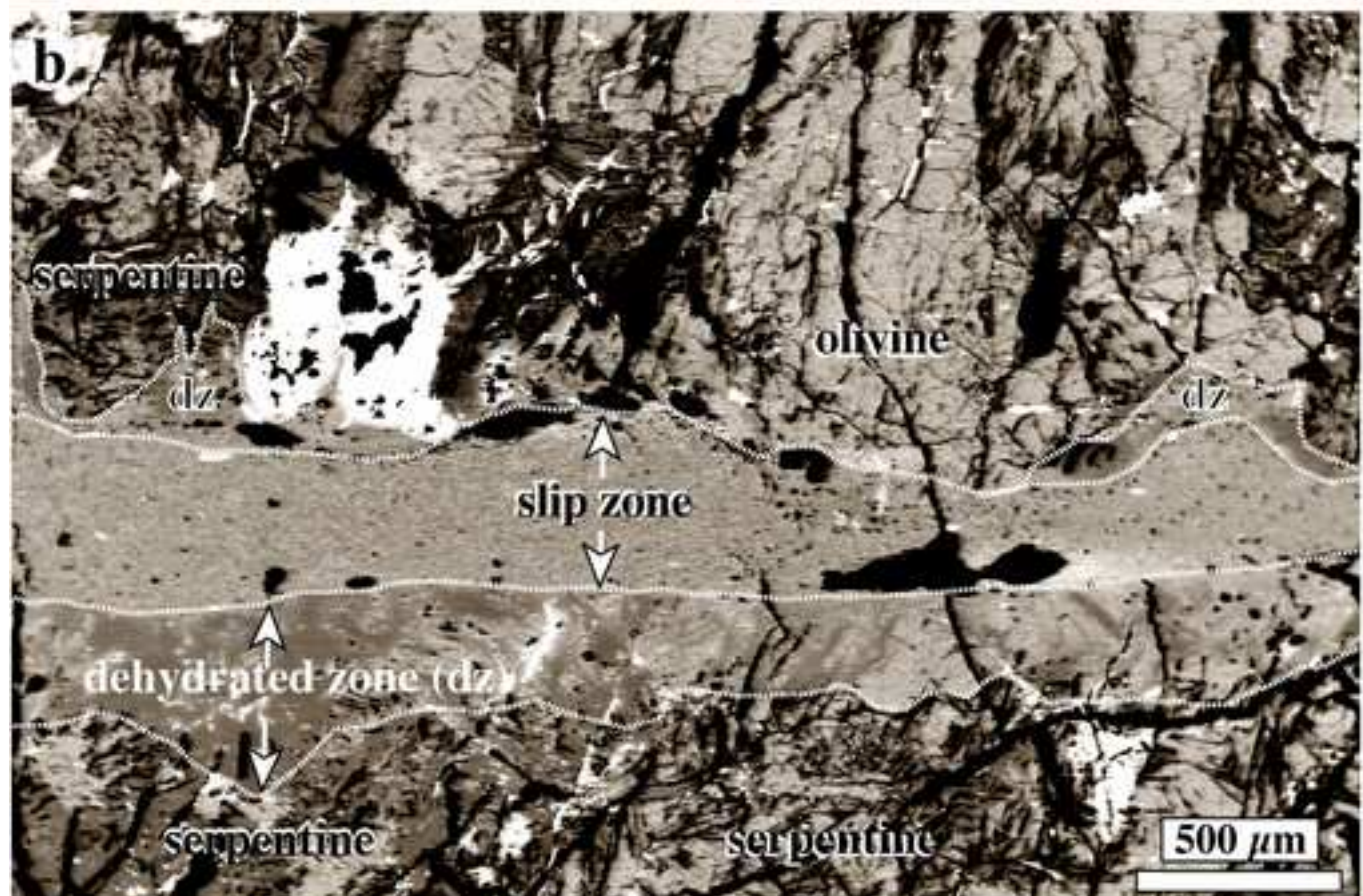
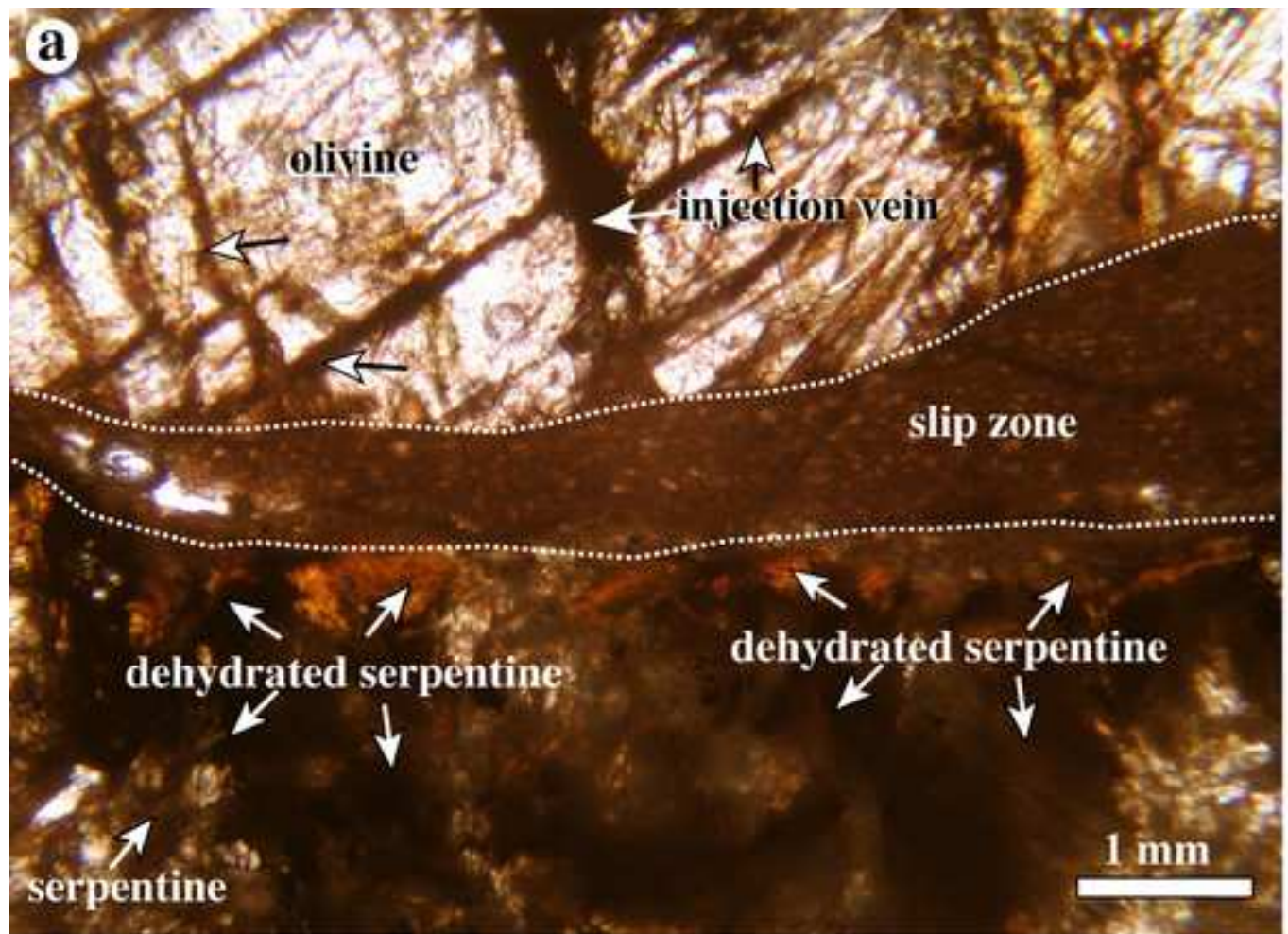


Figure6  
[Click here to download high resolution image](#)

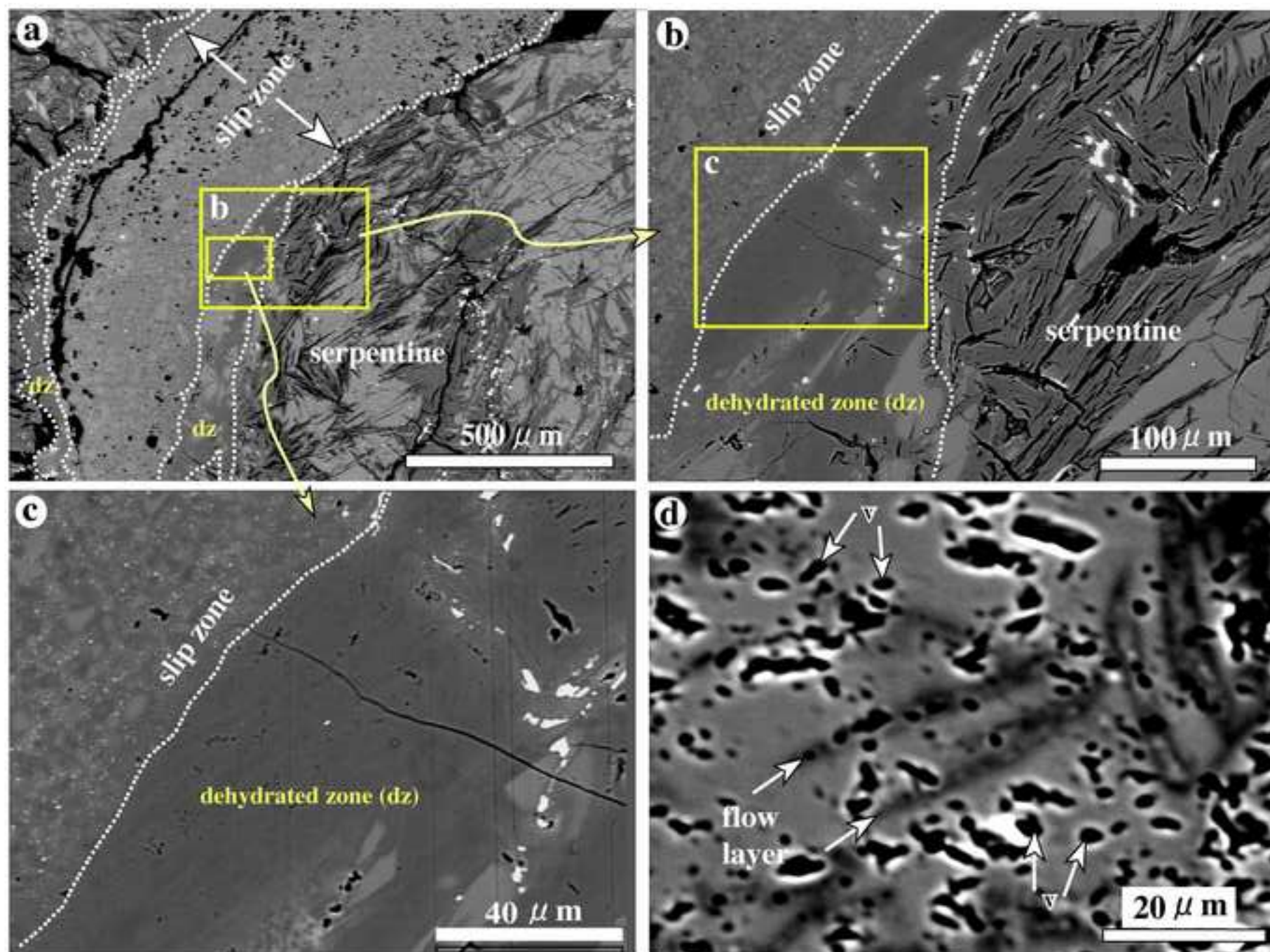


Figure7  
[Click here to download high resolution image](#)

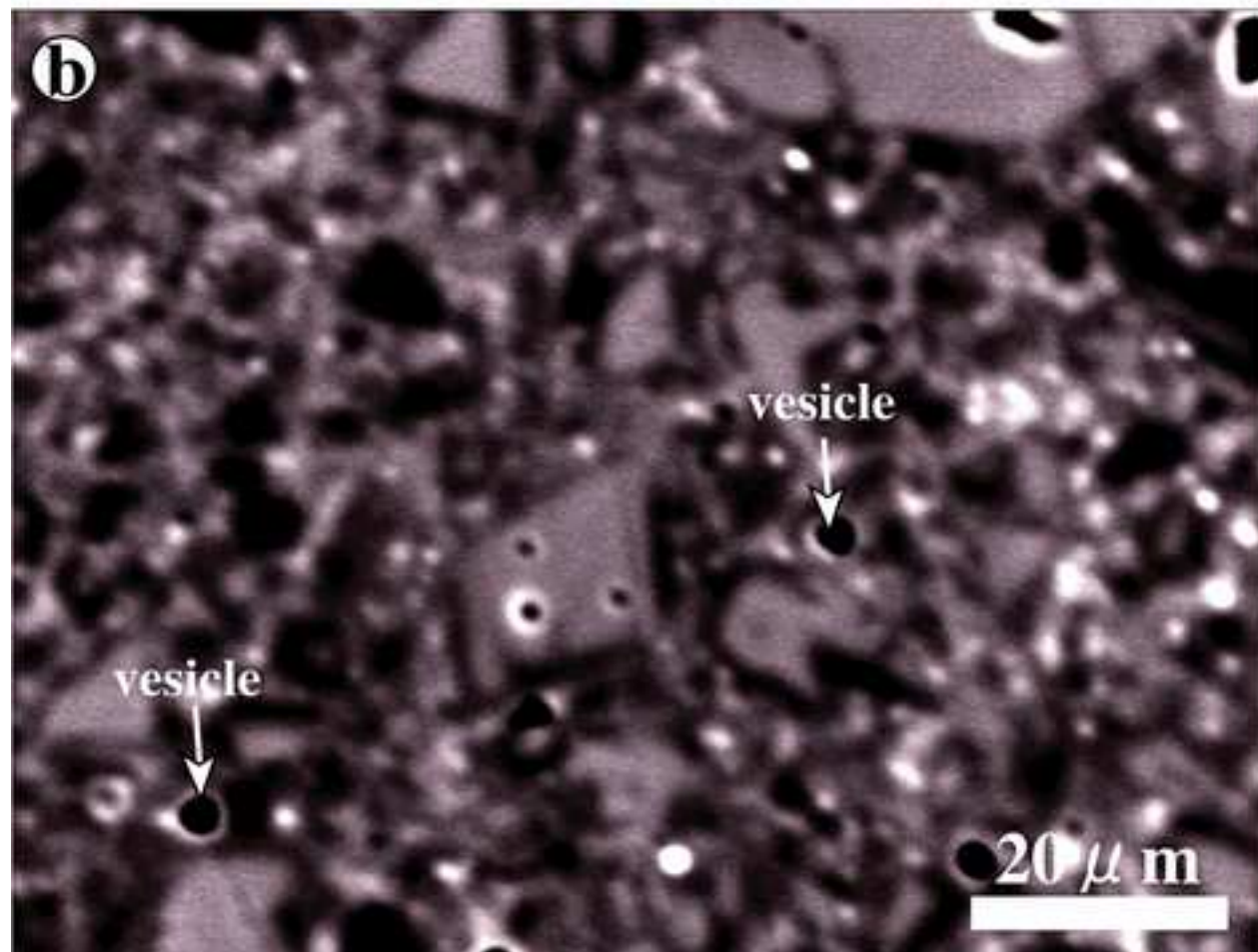


Figure8

[Click here to download high resolution image](#)

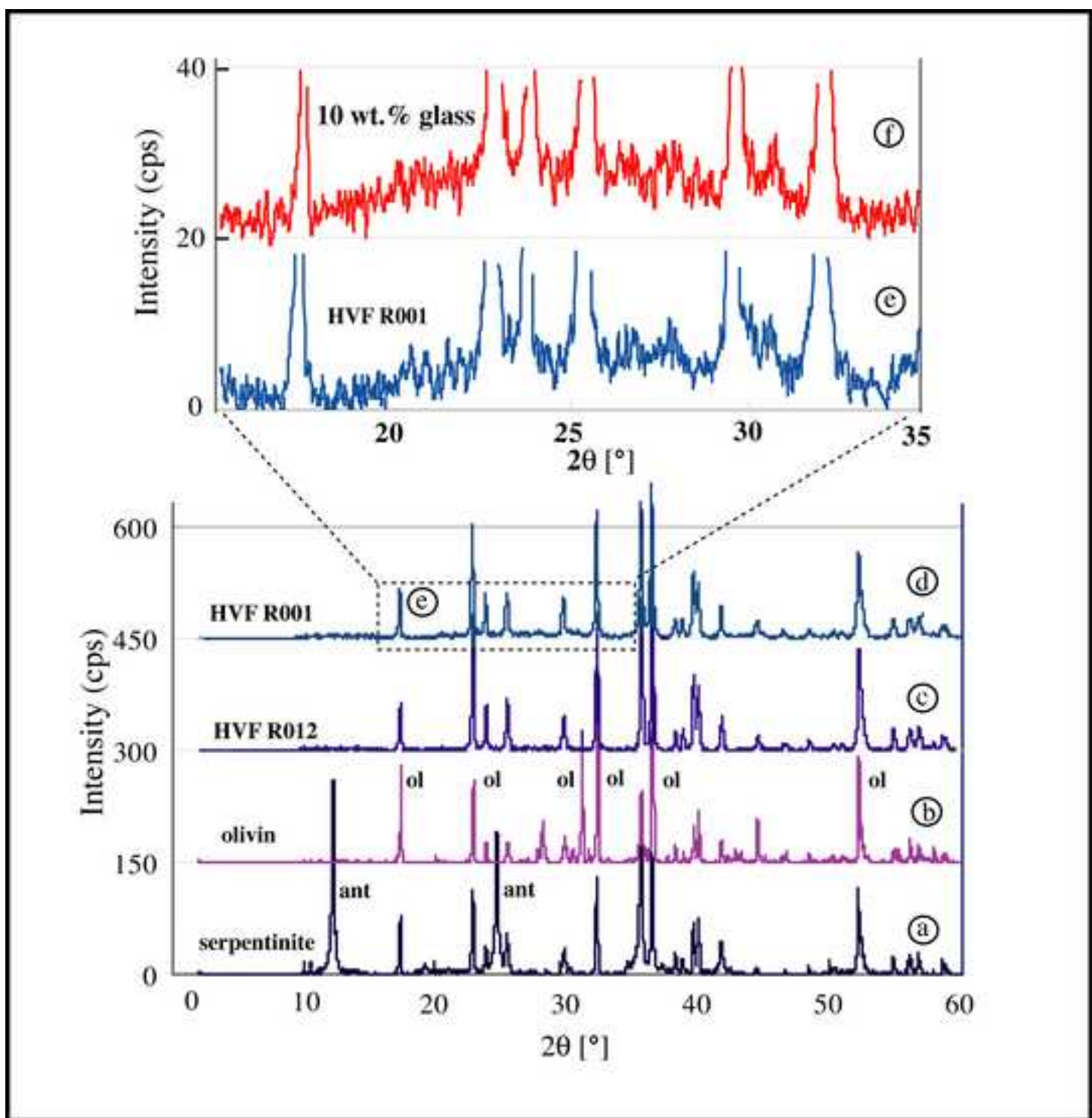


Figure9

[Click here to download high resolution image](#)

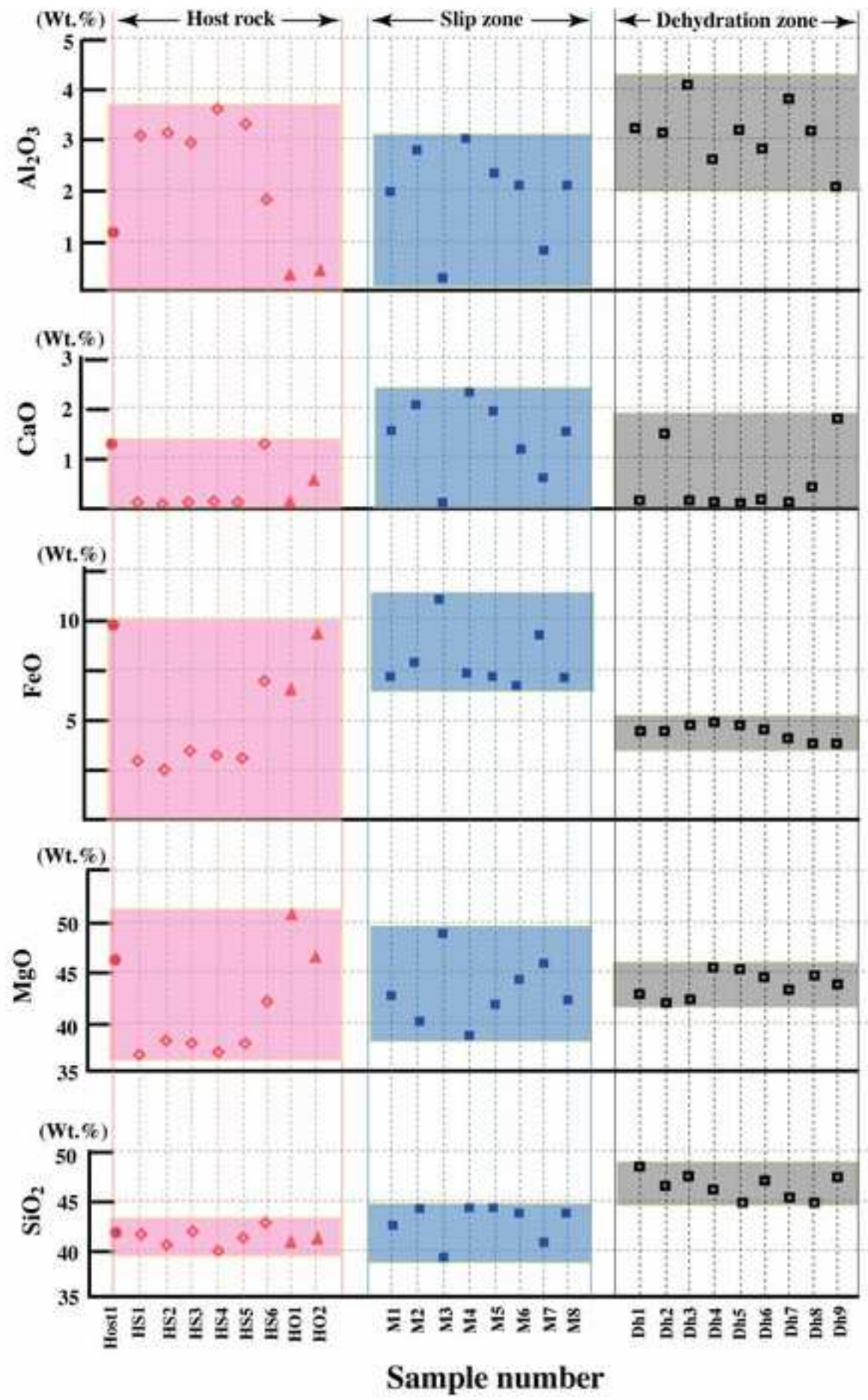




Figure10

[Click here to download high resolution image](#)

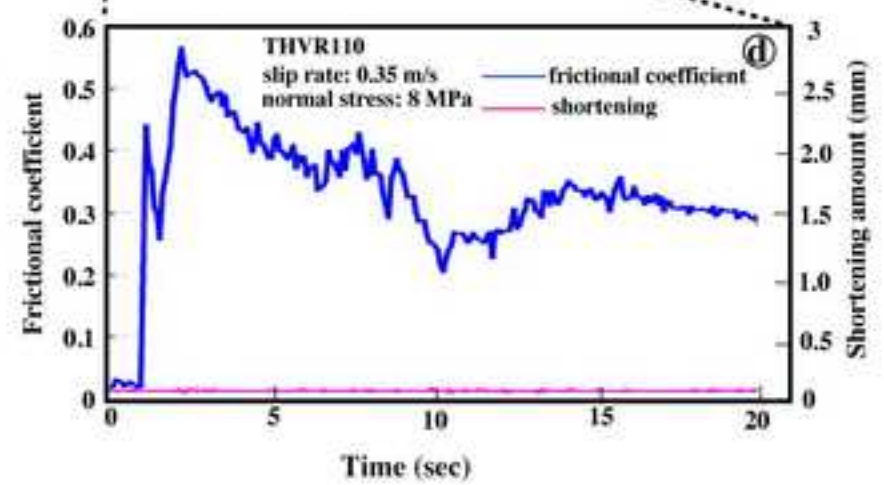
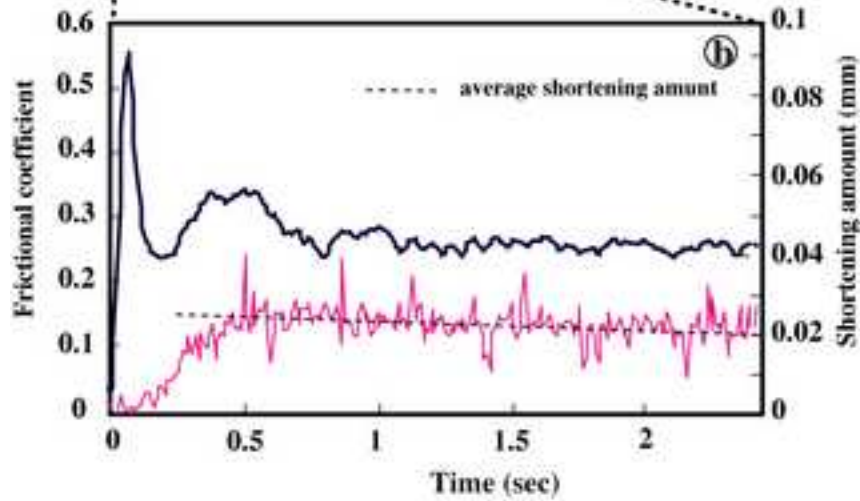
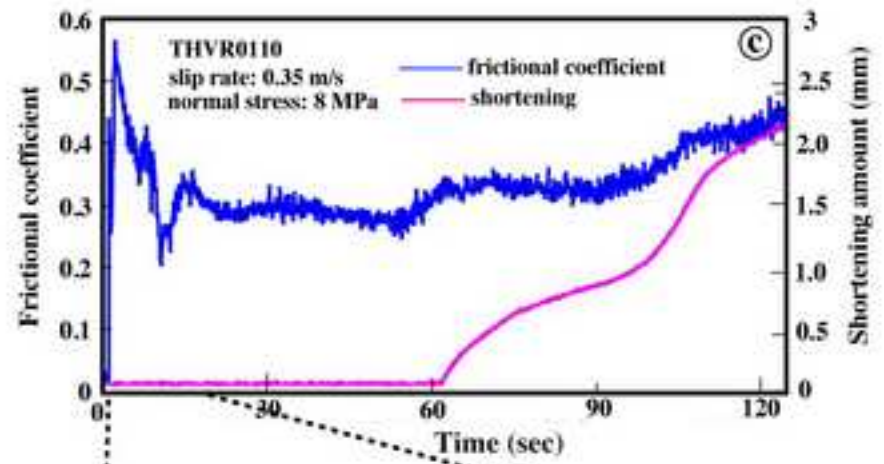
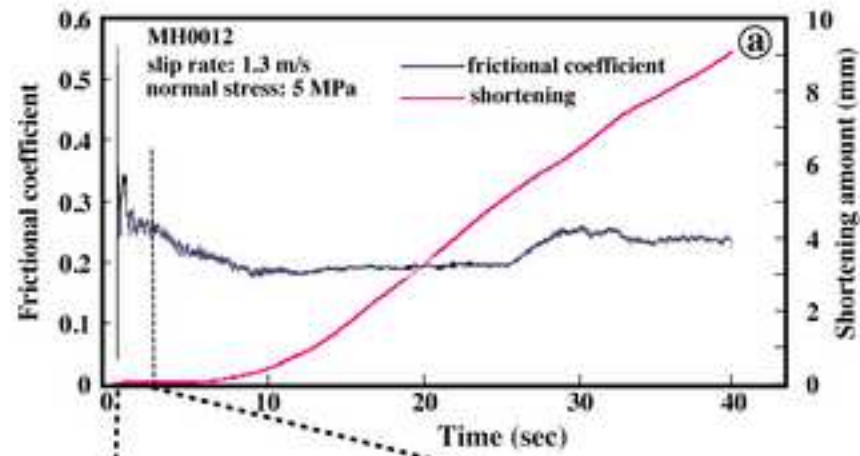


Figure11  
[Click here to download high resolution image](#)

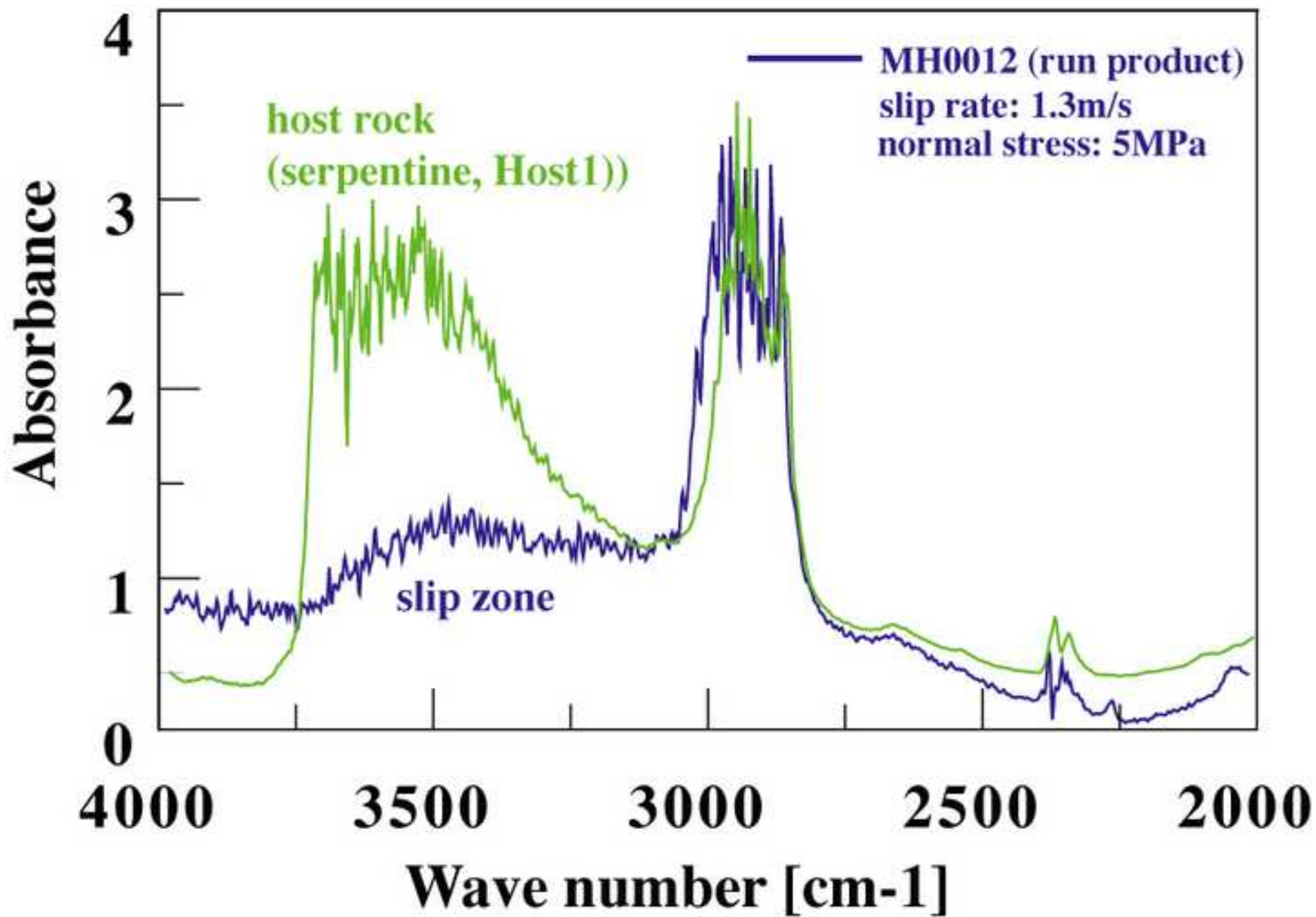


Figure12

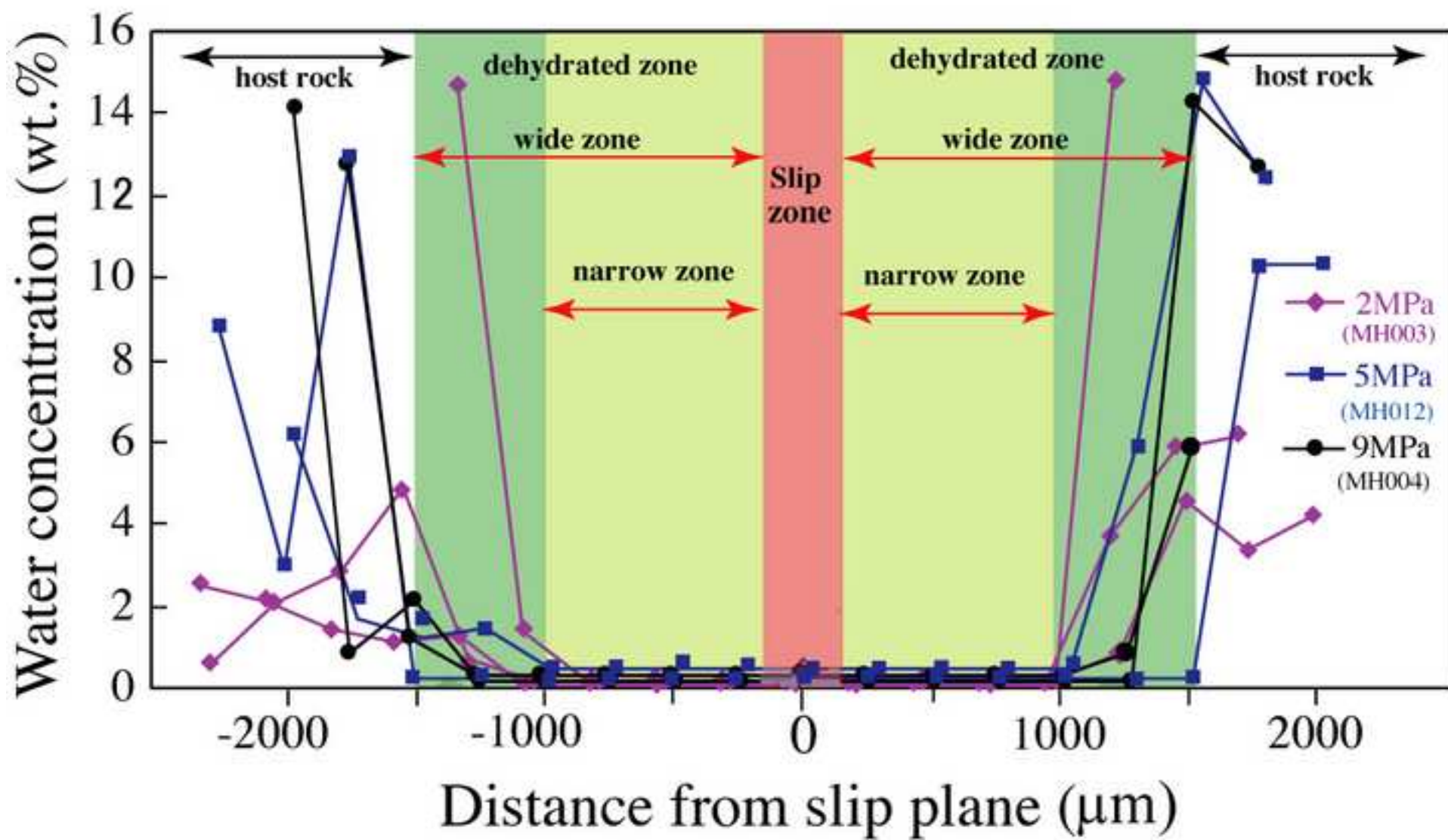
[Click here to download high resolution image](#)

Figure13  
[Click here to download high resolution image](#)

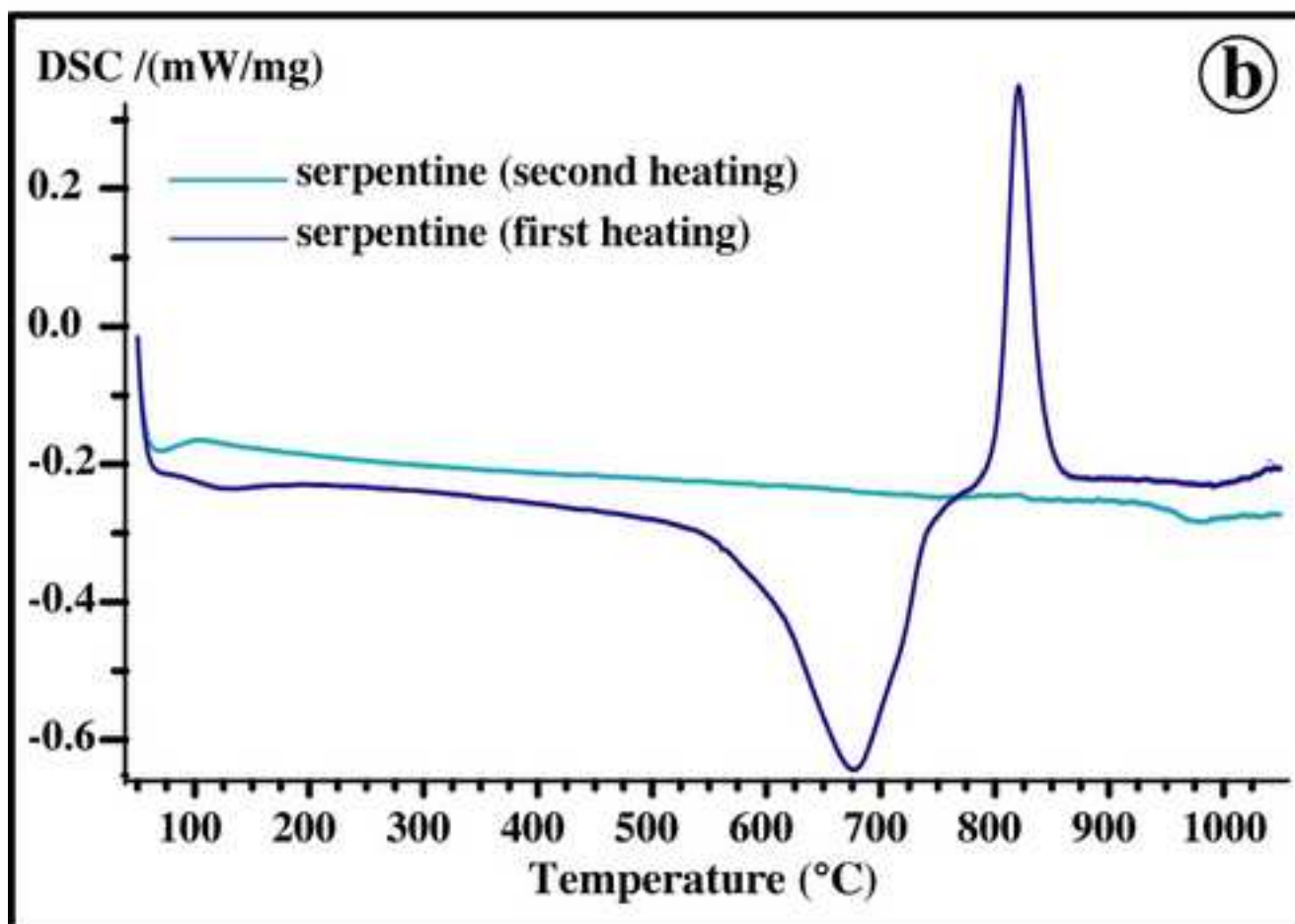
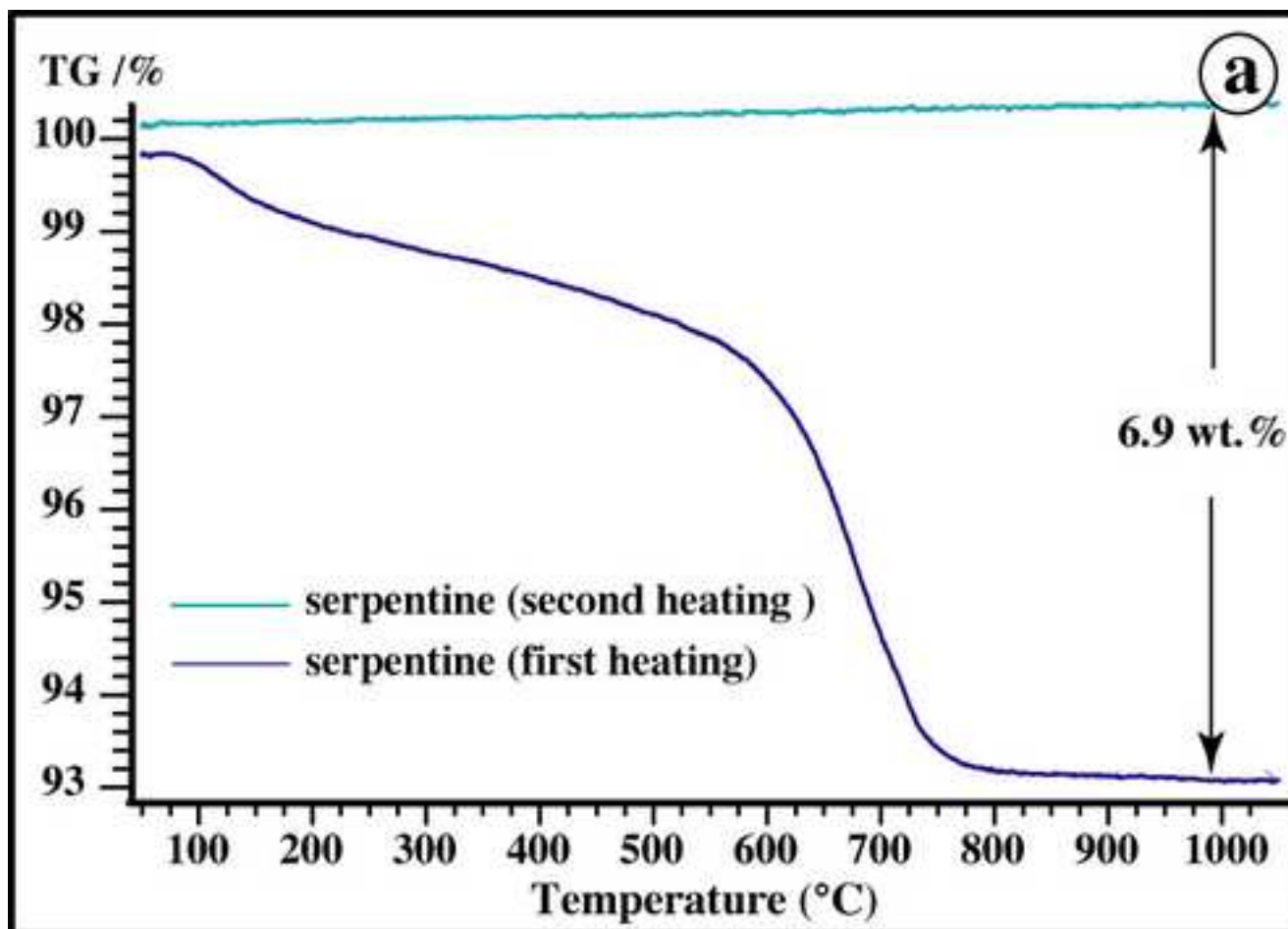


Figure14

[Click here to download high resolution image](#)

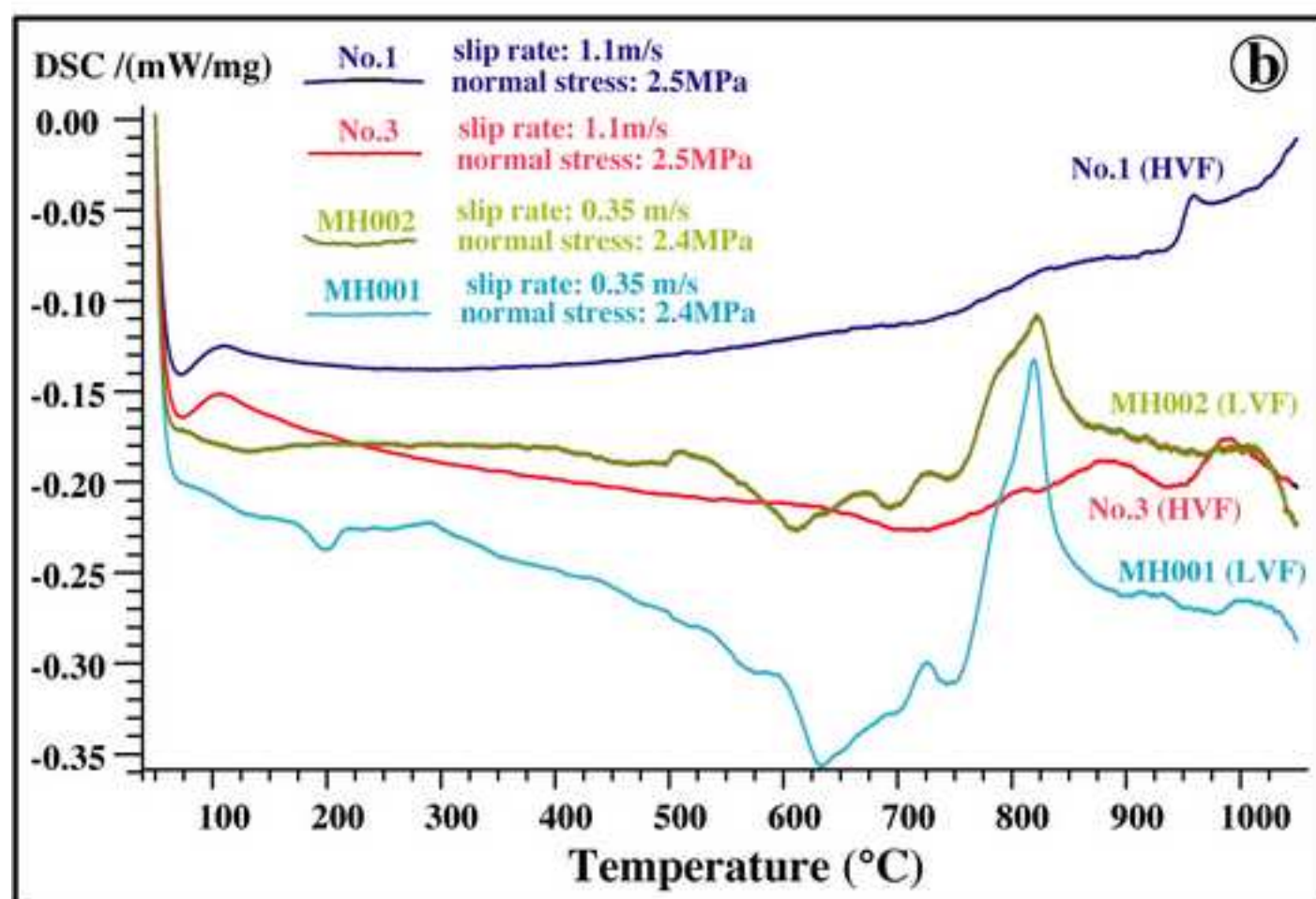
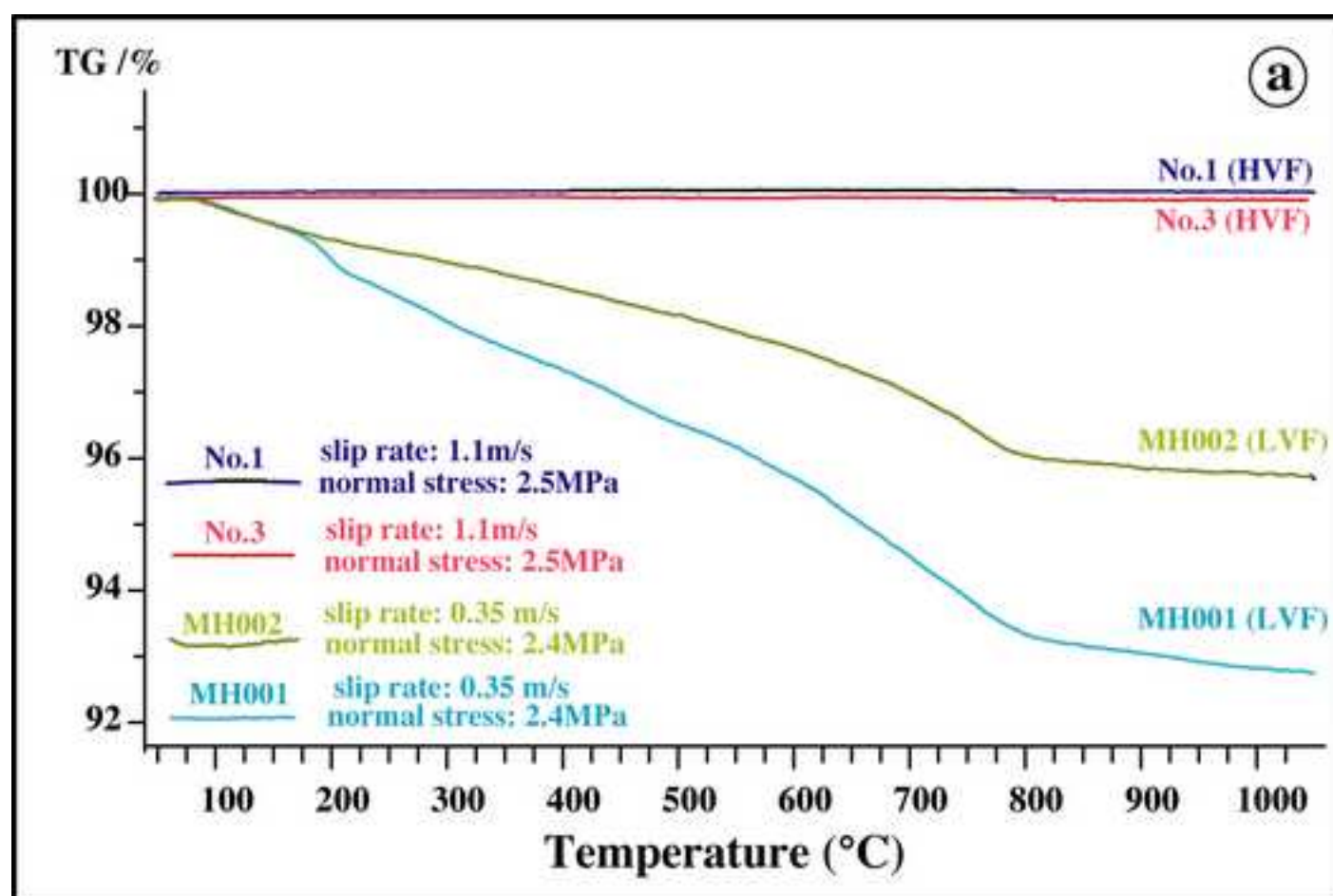


Table 1. Run products used for microscopic analyses.

<u>Run number</u>	<u>Normal stress (MPa)</u>	<u>Slip rate (m/s)</u>	<u>Analytical method</u>
No.1	2.5	1.10	TG-DSC analysis
No.3	2.5	1.10	TG-DSC analysis
MH001	2.4	0.35	TG-DSC analysis
MH002	2.4	0.35	TG-DSC analysis
MH003	2	1.10	FTIR analysis
MH004	9	1.10	FTIR analysis
MH012	5	1.31	FTIR analysis
HVF R001	6.5	1.10	Powder X-Ray analysis, EPMA
HVF R007	4	1.31	Powder X-Ray analysis, EPMA
THVR110	8.1	0.35	Frictional coefficient, shortening
HVF R012	5	1.31	Powder X-Ray analysis, EPMA

Table 2. Compositions of host rock (Host1, XRF) and serpentine (HS1-HS6, EPMA) and olivine (HO1-HO2, EPMA) materials in the host rock.

Sample No.	Host1	HS1	HS2	HS3	HS4	HS5	HS6	HO1	HO2
SiO <sub>2</sub>	41.580	41.322	40.648	41.944	40.068	41.422	42.828	40.576	41.185
TiO <sub>2</sub>	0.000	0.196	0.199	0.196	0.19	0.191	0.002	0.002	0.011
Al <sub>2</sub> O <sub>3</sub>	1.098	3.076	3.104	2.919	3.610	3.224	1.777	0.175	0.800
FeO	9.904	3.063	2.887	3.674	3.268	3.225	7.074	6.327	9.335
MnO	0.228	0.137	0.170	0.181	0.14	0.166	0.127	0.140	0.181
MgO	45.908	36.694	38.194	37.997	37.141	38.112	43.460	51.206	46.294
CaO	1.242	0.106	0.114	0.106	0.095	0.088	1.260	0.127	0.526
Na <sub>2</sub> O	0.034	0.086	0.108	0.093	0.125	0.111	0.074	0.010	0.036
K <sub>2</sub> O	0.012	0.060	0.063	0.059	0.073	0.065	---	0.011	0.010
V	0.029	0.213	0.185	0.211	0.208	0.211	---	0.026	0.002
Cr <sub>2</sub> O <sub>3</sub>	---	1.284	1.089	0.593	1.026	1.098	0.509	0.103	0.153
NiO	0.398	0.352	0.35	0.364	0.307	0.308	0.326	0.311	0.319
Total	99.973	86.588	87.11	88.337	86.249	88.219	97.438	99.013	98.852

XRF: X-ray fluorescence analysis; EPMA: Electron microprobe analysis;

FeO\*: all Fe...; -not measured

Table 3. Chemical compositions of molten materials derived from the slip zone (M1-M8, EPMA).

Sample No.	M1	M2	M3	M4	M5	M6	M7	M8
SiO <sub>2</sub>	42.366	44.776	39.494	44.441	44.073	43.809	41.185	43.629
TiO <sub>2</sub>	0.015	0.012	0.001	0.025	0.022	0.003	0.011	0.000
Al <sub>2</sub> O <sub>3</sub>	1.971	2.814	0.000	3.010	2.371	2.003	0.800	2.044
FeO*	7.144	7.860	11.243	7.465	7.289	6.704	9.335	7.391
MnO	0.081	0.077	0.207	0.095	0.141	0.080	0.181	0.103
MgO	43.176	40.053	48.68	38.99	42.037	44.681	46.294	42.209
CaO	1.595	2.020	0.014	2.275	1.953	1.138	0.526	1.422
Na <sub>2</sub> O	0.126	0.126	0.003	0.159	0.139	0.097	0.036	0.076
K <sub>2</sub> O	0.006	0.005	0.002	0.011	0.000	0.000	0.010	0.014
V	0.035	0.034	0.029	0.024	0.003	0.022	0.002	0.015
Cr <sub>2</sub> O <sub>3</sub>	0.324	0.403	0.000	0.537	0.650	0.655	0.153	0.459
NiO	0.350	0.284	0.398	0.295	0.228	0.254	0.319	0.292
Total	97.188	98.464	99.558	97.328	98.908	99.446	98.852	97.654

EPMA: Electron microprobe analysis;

FeO\*: all Fe



Table 4. Chemical compositions of serpentine minerals in the dehydration zones (Dh1-Dh9, EPMA).

Sample No.	Dh1	Dh2	Dh3	Dh4	Dh5	Dh6	Dh7	Dh8	Dh9
SiO <sub>2</sub>	47.462	45.76	46.881	45.543	44.184	46.035	44.832	44.243	46.742
TiO <sub>2</sub>	0.000	0.011	0.025	0.000	0.013	0.000	0.005	0.003	0.000
Al <sub>2</sub> O <sub>3</sub>	3.198	3.107	4.020	2.549	3.123	2.768	3.813	3.116	1.998
FeO*	4.023	4.245	4.482	4.225	4.059	3.978	4.016	3.826	3.794
MnO	0.031	0.054	0.031	0.035	0.012	0.031	0.030	0.050	0.027
MgO	43.347	42.058	42.198	45.431	45.116	44.074	43.134	44.208	43.458
CaO	0.249	1.424	0.056	0.027	0.018	0.015	0.048	0.398	1.797
Na <sub>2</sub> O	0.033	0.054	0.041	0.028	0.028	0.024	0.063	0.113	0.121
K <sub>2</sub> O	0.000	0.010	0.004	0.000	0.012	0.002	0.001	0.005	0.013
V	0.024	0.020	0.034	0.018	0.025	0.018	0.040	0.030	0.001
Cr <sub>2</sub> O <sub>3</sub>	0.419	0.236	0.870	0.463	0.889	0.476	1.441	1.605	0.621
NiO	0.151	0.160	0.134	0.181	0.214	0.165	0.223	0.157	0.163
Total	98.936	97.139	98.777	98.500	97.693	97.586	97.646	97.755	98.735

EPMA: Electron microprobe analysis;

FeO\*: all Fe